Technical design and performances of the NEMO 3 detector

R. Arnold [a], C. Augier [b]⋆, J. Baker [c], A. Barabash [d], V. Brudanin [e], A.J. Caffrey [c], D. Dassié [f], V. Egorov [e], K. Errahmane [b], A.I. Etienvre [b], J.L. Guyonnet [a], F. Hubert [f], Ph. Hubert [f], C. Jollet [a], S. Jullian [b], I. Kisel [e], A. Klimenko [e], O. Kochetov [e], V. Kovalenko [e], D. Lalanne [b], F. Leccia [f], C. Longuemare [g], Ch. Marquet [f], F. Mauger [g], I. Nemchenok [e], H.W. Nicholson [h], I. Nikolic-Audit [f], H. Ohsumi [i], F. Piquemal [f], J.L. Reyss [j], X. Sarazin [b], L. Simard [b], Y. Shitov [e], A. Smolnikov [e], I. Štekl [k], J. Suhonen [l], C.S. Sutton [h], G. Szklarz [b], V. Timkin [e], V. Tretyak [e], V. Umatov [d], L. Vála [b,k], I. Vanushin [d], S. Vasiliev [e], V. Vasilyev [d], V. Vorobel [m], Th. Vylov [e]

[a] *IReS, IN2P3-CNRS et Université Louis Pasteur, 67037 Strasbourg, France*

[b] *LAL, IN2P3-CNRS et Université de Paris-Sud, 91405 Orsay, France*

[c] *INEEL, Idaho Falls, ID 83415, U.S.A.*

[d] *ITEP, 117259 Moscow, Russia*

[e] *JINR, 141980 Dubna, Russia*

[f] *CENBG, IN2P3-CNRS et Université de Bordeaux I, 33170 Gradignan, France*

[g] *LPC, IN2P3-CNRS et Université de Caen, 14032 Caen, France*

[h] *MHC, South Hadley, Massachusetts 01075, U.S.A.*

[i] *Saga University, Saga 840-8502, Japan*

[j] *LSCE, CNRS, 91190 Gif-sur-Yvette, France*

[k] *CTU, Prague, Czech Republic*

[ℓ] *JYVÄSKYLÄ University, 40351, Jyväskylä, Finland*

[m] *Charles University, Prague, Czech Republic*

Abstract

The development of the NEMO 3 detector, which is now running in the Fréjus Underground Laboratory (L.S.M. Laboratoire Souterrain de Modane), was begun more than ten years ago. The NEMO 3 detector uses the tracking-calorimeter technique in order to investigate double beta decay processes for several isotopes. The technical description of the detector is followed by the presentation of its performances.

Key words: NEMO, double beta decay, neutrino, Majorana, tracking detector, calorimeter
PACS: code pacs 1, code pacs 2

Contents

[1] Corresponding author, e-mail: augier@lal.in2p3.fr

1 Introduction

1.1 Objective of the experiment

The primary objective of the NEMO 3 experiment is to search for neutrinoless double beta decay for several isotopes. This research is one of the most pressing topics in neutrino physics, for which there is the fundamental problem of whether or not neutrinos are massless. If double beta decay without neutrino emission, $\beta\beta0\nu$, is observed the neutrino can be a massive Majorana particle, which is its own antiparticle.

It was proposed years ago [1] that there could be an exchange of neutrinos between two neutrons in the same nucleus leading to the emission of two electrons and no neutrinos. The Majorana mass term enables such a transition through a $V-A$ interaction. The observation of the $\beta\beta0\nu$ process would then prove the Majorana nature of the neutrino.

It is also possible to investigate $\beta\beta0\nu$ transitions to the 2^+ excited state, which involves a Majorana mass term through the $V+A$ interaction. Other mechanisms may contribute to the $\beta\beta0\nu$ process, in particular the emission of a Majoron, the boson associated with spontaneous symmetry breaking of lepton number. The search for the $\beta\beta M^0$ process involves a three body decay spectrum with the Majoron avoiding detection, which imposes additional constraints on the design of the detector. The objective of the NEMO 3 experiment (Neutrino Ettore Majorana Observatory) is to investigate these three decay modes to further the understanding of double beta decay.

In all double beta decays, which are second order weak interactions, nuclei decay into daughter nuclei by emitting two electrons accompanied by two undetected neutrinos. This is the $\beta\beta2\nu$ process which has already been observed for 10 isotopes: ^{48}Ca, ^{76}Ge, ^{82}Se, ^{96}Zr, ^{100}Mo, ^{116}Cd, ^{128}Te, ^{130}Te, ^{150}Nd and ^{238}U (see [2] for a review article).

The NEMO 3 experiment aims to search for the effective Majorana neutrino down to a mass $\langle m_\nu \rangle$ at the level of 0.1 eV. If only a limit is reached on the $\beta\beta0\nu$ half-life, an upper limit on $\langle m_\nu \rangle$ can be inferred from the relation

$$(T^{0\nu}_{1/2})^{-1} = (\langle m_\nu \rangle \,/\, m_e)^2 \times |M_{0\nu}|^2 \times F_{0\nu} \tag{1}$$

where $F_{0\nu}$ is the phase-space factor that is analytically calculated and proportional to the transition energy $Q^5_{\beta\beta}$. $M_{0\nu}$ is the nuclear matrix element of the relevant isotope for which calculations have large theoretical uncertainties. Given the uncertainty in $M_{0\nu}$, a mass limit of 0.1 eV corresponds to a neutrinoless double beta decay with a half-life limit of the order of 10^{25} years for ^{100}Mo. To improve the sensitivity of a double beta decay experiment it is preferable to study an isotope with larger $Q_{\beta\beta}$, not only to get a larger $F_{0\nu}$, but also to reduce the background in the search for a $\beta\beta 0\nu$ signal.

Measurements of a half-life as long as 10^{25} years is challenging. It requires a solid understanding of natural and cosmogenic radioactive backgrounds in the materials from which the detector is made and backgrounds induced by the radioactivity from the walls and atmosphere in the underground laboratory. Two prototypes, NEMO 1 [3] and NEMO 2 [4], were constructed and run to demonstrate the feasibility of the experimental technique. The development of NEMO 3 was begun more than ten years ago [5]. It reflects a more than 10-fold enhancement on the NEMO 2 sensitivity in order to measure the double beta decay half-life limits of 10^{25} yr for the $\beta\beta 0\nu$ process, 10^{23} yr for the $\beta\beta M^0$ process, and 10^{22} yr for the $\beta\beta 2\nu$ process.

1.2 General description of the NEMO 3 detector

The NEMO 3 philosophy is based on the direct detection of the two electrons from $\beta\beta$ decay by a tracking device and a calorimeter. The NEMO 3 detector, for which the general layout is shown in the Fig. 1, is similar in function to the earlier prototype detector, NEMO 2, but has lower radioactivity and is able to accommodate at least 10 kg of double beta decay isotopes.

The NEMO 3 detector is now installed in the Fréjus Underground Laboratory (LSM [2]). It is cylindrical in design and divided into 20 equal sectors, as shown in Fig. 2. The segmentation permits easy access to a patchwork of source foils of the different isotopes to be studied. This patchwork is also cylindrical in form. It is 3.1 m in diameter, 2.5 m in height and $30 - 60$ mg/cm^2 thick.

The source foils are fixed vertically between two concentric cylindrical tracking volumes composed of 6180 open octagonal drift cells. The drift cells are 270 cm long, operating in Geiger mode at 7 mbar above atmospheric pressure, with a partial pressure of 40 mbar of alcohol in a mixture of helium gas and ethyl alcohol. The cells run vertically and three-dimensional tracking is accomplished with the arrival time of the signal on the anode wire and the plasma propagation times to the ends of the drift cells.

Energy and time-of-flight measurements are acquired from plastic scintillators

[2] Laboratoire Souterrain de Modane

covering the two vertical surfaces of the active tracking volume. To further enhance the acceptance efficiency, the endcaps (the top and bottom of the detector) are also equipped with scintillators in the spaces between the Geiger cell layers. This calorimeter is made of 1940 large blocks of scintillators coupled to very low radioactivity 3" and 5" PMTs. The 10 cm thick blocks of scintillator yield a high photon detection efficiency.

A solenoid surrounding the detector produces a 25 Gauss magnetic field parallel to the foil axis, in order to discriminate against the particle charge. (e^+e^-) pairs are produced in the source foils in the 1 to 10 MeV region by high-energy gamma rays present in the detector from neutron capture. The curvature measurements also permit an efficient rejection of incoming electrons.

Finally, an external shield, in the form of 20 cm of low radioactivity iron, covers the detector to reduce γ-rays and thermal neutron fluxes. Outside of this iron there is a borate water shield to thermalize fast neutrons and capture thermal neutrons.

In the NEMO 3 detector, electrons, positrons, photons and delayed-α particles can be identified. Thus, the detector is able to detect multi-particle events in the low energy domain of natural radioactivity.

1.3 Background of the experiment

The most significant concern in this double beta decay experiment is background. The calorimeter measures the energy of the two electrons emitted from a common vertex in the source foil. The energy region of interest for the $\beta\beta0\nu$ signal is around 3 MeV ($Q_{\beta\beta}(^{100}\text{Mo})$ = 3.034 MeV and $Q_{\beta\beta}(^{82}\text{Se})$ = 2.995 MeV [6]). This energy region is shared by some energetic natural radioactivity, which can produce two electrons in the source which mimic $\beta\beta0\nu$ decays. The key to the success of the experiment is to be able to positively identify these background events with high efficiency.

1.3.1 Natural radioactivity decay chains and other radioactive isotopes

In general, natural radioactivity coming from very long half-life isotopes such as potassium (K), uranium (U) and thorium (Th) needs to be carefully monitored. The decay chain for ^{235}U is not taken into account, because even though the half-life is $7.04{\cdot}10^8$ yr its natural isotopic abundance is only 0.7% and its decay chain daughter nuclei do not generate enough energy to mimic the $\beta\beta0\nu$ signal. Concerning ^{40}K, the energy range of these decays is again not a background concern for the $\beta\beta0\nu$'s signal.

From the natural decay chains of ^{238}U and ^{232}Th, only ^{214}Bi and ^{208}Tl are β-decay isotopes with Q_β greater than 3 MeV (with respective Q_β values of 3.270 and 4.992 MeV, and respective half-lives of 19.9 and 3.05 minutes [7]). Thus, ^{214}Bi and ^{208}Tl produce γ-rays and electrons that are energetic enough to simulate $\beta\beta0\nu$ events at 3 MeV (energies and intensities of γ-rays from natural radioactivity decay chains of ^{238}U and ^{232}Th can be found in Ref. [8]). The most energetic γ-rays are from ^{208}Tl, for which the branching ratio is 36% at 2.615 MeV.

Radon ^{222}Rn ($T_{1/2}$ = 3.824 days) and thoron ^{220}Rn ($T_{1/2}$ = 55.6 s) are α-decay isotopes, which have ^{214}Bi and ^{208}Tl daughter isotopes respectively. Coming mainly from rocks and present in the air, these are very diffusion prone rare gases which can enter the detector. Subsequent α-decay of these gases gives ^{218}Po and ^{216}Po respectively, which can contaminate the interior of the detector.

1.3.2 External and internal backgrounds

When describing the background, it is convenient to distinguish between the "internal" and "external" sources. The internal backgrounds come from radioactive contaminants inside the $\beta\beta$ source foil, while external backgrounds come from radioactive contaminants outside the $\beta\beta$ source foils, which interact with the detector, such as the materials used in constructing the detector or activity in the laboratory walls and air. The external background is defined as events produced by γ-ray sources located outside the source foils and interacting with them. The interaction of gammas in the foil can lead to two electron-like events by e^+e^- pair creation, double Compton scattering or Compton followed by Möller scattering.

One of the main sources of this external radioactivity comes from the PMTs, but there are other sources too, such as cosmic rays, radon and neutrons. To decrease the background for the NEMO 3 detector it is placed at a depth of 4800 m water equivalent, where cosmic ray effects have been found to be negligible. The low activity iron shield reduces the flux of γ-rays and neutrons. A magnetic field and additional shields of borated water, wood and paraffin suppress the backgrounds from fast and slow neutrons. The vigorous air ventilation system in the laboratory reduces radon levels down to 10-20 Bq/m^3. All the materials used in the detector have been selected for their radiopurity properties and in particular, a great effort has been made to reduce the contamination inside the PMTs from ^{40}K, ^{214}Bi and ^{208}Tl.

The internal background for the $\beta\beta0\nu$ signal in the 3 MeV region has two origins. The first is the tail of the $\beta\beta2\nu$ decay distribution of the source, which cannot be separated from the $\beta\beta0\nu$ signal and the level of overlap depends on the energy resolution of the detector. Thus, this ultimately defines the half-life limits to which the $\beta\beta0\nu$ can be searched for. The second background comes from the β decays of ^{214}Bi and ^{208}Tl, which are present in the source at some level. They can mimic $\beta\beta$ events by three mechanisms. These are β decay accompanied by an electron conversion process, Möller scattering of β-decay electrons in the source foil and β-decay emission to an excited state followed by a Compton scattered γ-ray. The two last mechanisms can be detected as two electron events if the γ-ray is not detected. Thus, the experiment requires ultra-pure source foils. The maximum levels of impurities in the source have been calculated so as to produce fewer events than the tail of the $\beta\beta2\nu$ decay gives in the region of interest for $\beta\beta0\nu$.

Consequently, in the construction of the NEMO 3 experiment every attempt has been made to minimize external and internal backgrounds by purification of the enriched isotope samples and by carefully selecting all the detector materials. Furthermore, as it has been shown with the NEMO 2 prototype, NEMO 3 will be able to characterize and measure its own background.

2 Technical design of the NEMO 3 detector

2.1 The NEMO 3 sources

2.1.1 Introduction

The primary design feature of the NEMO 3 experiment was to have the detector and the source of the double beta decay separated, unlike the case of the ^{76}Ge experiments. This permits one to study several double beta decay isotopes. This point is critical if one is to confirm an excess of events from one isotope with another isotope. It also reduces the dependence of the interpretation of the result on the nuclear matrix elements. Furthermore, a rich study of the backgrounds and systematic effects is possible.

The choice of which nuclei to study was affected by several parameters. These include, but are not limited to, the transition energy ($Q_{\beta\beta}$), the nuclear matrix elements ($M_{0\nu}$ and $M_{2\nu}$) of the transitions for $\beta\beta0\nu$ and $\beta\beta2\nu$ decays, the background in the energy region surrounding the $Q_{\beta\beta}$ value, the possibility of reducing the radioactivity of the isotope studied to acceptable levels, and finally the natural isotopic abundance of the candidate. Basing the choice singularly on $M_{0\nu}$ is not advisable because the calculations are too uncertain. A good indicator is the $Q_{\beta\beta}$ value with respect to backgrounds. As explained in Section 1.3, the 2.615 MeV γ-ray produced in the decay of ^{208}Tl is consistently a troublesome source of background and it is important to select $\beta\beta$ candidates with a $Q_{\beta\beta}$ value above this transition. The natural isotopic abundance is another useful indicator because in general the higher the abundance the easier the enrichment process. Typically only isotopic abundances greater than 2% are considered. Five nuclei satisfy these two criteria: ^{116}Cd , ^{82}Se, ^{100}Mo, ^{96}Zr and ^{150}Nd (with respective $Q_{\beta\beta}$ values of 2804.7, 2995.2, 3034.8, 3350.0 and 3367.1 keV and respective abundance values of 7.5, 9.2, 9.6, 2.8 and 5.6% [6]). Given this list and the availability of ^{100}Mo, much effort has been focused by the NEMO collaboration on this nucleus (already measured by the NEMO 2 prototype [9]), but not exclusively, in view of the fact that the detector can house several different sources.

Because of ongoing improvements in the isotopic enrichment processing in Russia, where all double beta decay sources were produced, two isotopes have been added to the list of interesting sources, ^{130}Te and ^{48}Ca (with respective $Q_{\beta\beta}$ values of 2528.9 and 4272.0 keV and respective abundance values of 33.8 and 0.187% [6]). Note that ^{48}Ca fails to meet the abundance selection criterion but has an impressive $Q_{\beta\beta}$ value.

A description of the current population of the 20 sectors of NEMO 3 follows. To study the $\beta\beta0\nu$ processes 6914 g of ^{100}Mo and 932 g of ^{82}Se are housed in 12 and 2 sectors respectively. The objective here is to reach a sensitivity for the effective neutrino mass on the order of 0.1 eV. Several other double-β decay isotopes in smaller quantities have been introduced to study the $\beta\beta2\nu$ processes which will complement the very detailed studies provided by the ^{100}Mo and ^{82}Se on angular distributions and single electron energy spectra. This second tier of isotope samples consists of 454 g of ^{130}Te (2 sectors), 405 g of ^{116}Cd (1 sector), 37 g of ^{150}Nd, 9 g of ^{96}Zr and 7 g of ^{48}Ca. Finally, source foils with high levels of radiopurity and effectively void of internal backgrounds will measure the external background in the experiment. This not only accounts for the presence of 621 g of copper but also a very pure oxide of natural tellurium, which permits one to study the background near 3 MeV. The tellurium also provides an investigation of the $\beta\beta2\nu$ because the natural abundance of isotope 130 for tellurium is 34%, which gives 208 g of ^{130}Te. Historically this isotope has had two different geochemical half-life measurements and a reliable one is sought here.

For each sector, a source frame was constructed on which were placed seven strips. The mean length of the strips is 2480 mm with a width of 63 mm if they are on the edges of the frame or 65 mm for the five strips in the middle of the frame. All the strips are attached to the frames in a clean room at the LSM then introduced into the sectors. The so-called “NEMO 3 camembert”, depicts the distribution of the sources in the 20 sectors, Fig. 3.

The thickness of the source foils was chosen to take into account the energy resolution, which is fixed by the calorimeter design. The detector efficiency for $\beta\beta0\nu$ process is not compromised as long as the surface densities of the foils do not exceed 60 mg/cm^2. As a consequence the source foils have surface densities between 30 and 60 mg/cm^2, which means a thickness lower than 60 μm for the metallic foils (density of $\sim$ 10 g/cm^3) and lower than 300 μm for composite foils (density of $\sim$ 2 g/cm^3).

As stated earlier, NEMO 3 sources are metallic or composite. Cadmium, copper and part of the molybdenum are the metallic sources. Composite foils are a mixture of source powder and organic glue. 64% of ^{100}Mo is in the form of composite strips. The selenium, tellurium, zirconium, neodymium and calcium foils are also composite foils.

For composite foils, the glue is made from water and some percentage of PVA (polyvinyl alcohol). This mixture is laid down on a Mylar sheet and then covered by another sheet forming a sandwich-like structure. These sheets are often referred to as backing films, which provide mechanical rigidity. The Mylar sheets have undergone a special processing in which a large number of microscopic holes (around 0.4 μm in diameter) have been created to insure a good bond with the glue. The holes are made first by irradiating the Mylar at JINR with a ^{84}Kr ion beam of 3 MeV/nucleon in energy and a luminosity of around $5{\cdot}10^{11}$ ions/s. Nearly 30% of the backing film surface is affected by the ion tracks. The next step in preparing the film is chemically etching it with NaOH (5 Moles) at 70^o C, then the film is washed with water and 1% of CH_3COOH (acetic acid) and finally dried with hot air. There are three types of backing film used in the experiment. Type 1 has a thickness of 18 μm and around $7{\cdot}10^7$ holes/cm^2. Type 2 has a thickness of 19 μm and around $2{\cdot}10^7$ holes/cm^2. Type 3, which is 23 μm thick, has around $7{\cdot}10^7$ holes/cm^2. All the products (Mylar, water, acid...) used to process the backing film have been selected for their radiopurity with High Purity Germanium detector measurements at LSM (HPGe from Eurisys Mesures Company).

The characteristics of all the source foils' strips in the 20 sectors are summarized in Tables 1 and 2, where η is the percentage of $\beta\beta$ decay isotope in the enriched sample; M_1, M_2 and M_3 are respectively the **total** mass of material, the mass of the **element**, and the mass of the $\beta\beta$ decay **isotope** in the foil. In these tables, **(M)** and **(C)** are written respectively for metallic and composite foil.

2.1.2 Radiopurity of the sources with respect to ^{214}Bi and ^{208}Tl

As presented in section 1.3, the presence of impurities in the source foils may give rise to two-electron events which mimic $\beta\beta$ decay and produce background events in the region of the $\beta\beta0\nu$ signal. These impurities have been sufficiently reduced that given the energy resolution of the calorimeter, the ultimate background for the $\beta\beta0\nu$ signal is the tail of the $\beta\beta2\nu$ decay distribution. This is why acceptable levels of ^{214}Bi and ^{208}Tl in the foils, due to their large Q_β values, depends on the number of $\beta\beta2\nu$ events in the region 2.8 to 3.2 MeV. For 10 kg of ^{100}Mo ($Q_{\beta\beta} = 3.035$ MeV), 1 background event/yr is expected from the $\beta\beta2\nu$ process above 2.8 MeV. As a consequence, the maximum levels of ^{214}Bi and ^{208}Tl contamination in the Mo source have been calculated to ensure that $\beta\beta2\nu$ is the limiting background, that means that ^{214}Bi (and ^{208}Tl) should yield less than 0.4 background events/yr above 2.8 MeV for 10 kg of ^{100}Mo. The associated limits are thus:

$$A_{(^{100}\mathrm{Mo})}(^{214}\mathrm{Bi}) \ < \ 0.3 \ \mathrm{mBq/kg} \tag{2}$$

$$A_{(^{100}\mathrm{Mo})}(^{208}\mathrm{Tl}) \ < \ 0.02 \ \mathrm{mBq/kg} \tag{3}$$

For ^{82}Se the $T^{2\nu}_{1/2}$ is 10 times longer than for ^{100}Mo, however the available mass of this isotope is only 1 kg. Similarly, simulations have given the maximum levels of contamination for ^{214}Bi and ^{208}Tl in a 1 kg Se source foil:

$$A_{(^{82}\mathrm{Se})}(^{214}\mathrm{Bi}) \ < \ 0.7 \ \mathrm{mBq/kg} \tag{4}$$

$$A_{(^{82}\mathrm{Se})}(^{208}\mathrm{Tl}) \ < \ 0.05 \ \mathrm{mBq/kg} \tag{5}$$

No specification limits for activities of these contaminants were required for the other isotopes. Given the low mass of these isotopes, the limits obtained are not expected to be as competitive as for the Mo and Se.

2.1.3 Production and enrichment of molybdenum

The isotopic abundance of ^{100}Mo is 9.6% in ^{nat}Mo. Using enrichment processes in Russia under the control of ITEP, Mo samples with 95.14 to 98.95% enrichment in ^{100}Mo were produced having a total mass of 10 kg.

The enrichment process involves the production of MoF_6 gas from natural Mo. This gas is then centrifuged to isolate the heavier Mo isotopes such as ^{100}Mo. The next step is an oxidation-reduction reaction on the enriched $^{100}MoF_6$ gas which yields $^{100}MoO_3$ and finally ^{100}Mo metallic powder.

Radioactivity measurements of this enriched Mo powder have shown that the enrichment process must be complemented with a purification process, more specifically Thorium extraction. However the best measurements obtained with the HPGe spectrometer ($\sim$ $(1-8)$ mBq/kg for ^{214}Bi and $\sim$ $(0.4-2)$ mBq/kg for ^{208}Tl) did not satisfy the specific requirements for NEMO 3 given in Eq. 2 and Eq. 3. To reach these levels, the collaboration decided to investigate two different purification methods in parallel: a physical process and a chemical process. The methods were refined using samples of natural molybdenum. HPGe measurements were made before and after processing to identify improvements in the purification processes.

2.1.4 Physical purification of the enriched Mo powder and metallic strip fabrication

Enriched Mo powder is used directly to both purify and produce metallic foils. This purification process, developed by ITEP, involves transforming the powder into an ultrapure monocrystal with a mass of around 1 kg.

The powder is first pressed to obtain a solid Mo sample. Then the Mo is locally melted in a vacuum with an electron beam and a monocrystal is drawn from the liquid portion. Impurities coming from natural radioactivity decay chains make a migration towards the crystal extremities, because these are more soluble in the melting zone than molybdenum. Finally, cutting the outlines of the crystal and repeating the process, we obtain a very pure sample, from which an enriched purified Mo monocrystal can be grown, with a 20 mm diameter.

"Short" metallic strips, which are between 44 and 63 μm thick and between 64 and 1445 mm long, are fabricated from the cut monocrystal by heating and rolling it in a vacuum to avoid pollution. The next step is to trim the edges to obtain short strips 63 to 65 mm wide. Wastes from each step can be recycled, either by the physical or chemical method.

After the radioactivity measurements (see Table 3 for best limits), three to five short strips are attached end to end to create a NEMO 3 strip with a length of around 2500 mm. Seven of these NEMO 3 strips are installed in a frame to produce a source foil for one sector.

Metallic Mo strips were placed in sectors 02, 03 and 04. There are also five additional strips in sector 01 and two strips in sector 05, which give a combined mass of (2479 ± 5) g of ^{100}Mo.

2.1.5 Chemical purification of the enriched Mo powder and fabrication of composite strips

It is important to rid the source sample of all long lived naturally occurring radioactive isotopes. These one are U, Th and Ra [7]. This is in order to avoid the background coming from the decay of the short lived daughter products ^{214}Bi (from ^{226}Ra with half-life of 1600 yr) and ^{208}Tl (from ^{232}Th and ^{228}Th, and from ^{228}Ra with half-life of 5.75 yr).

The chemical purification process takes advantage of an equilibrium break of ^{238}U and ^{232}Th decay chains, which can selectively transform these chains to non-equilibrium states in which only short lifetime daughters exist. The purification process was carried out in a class 100 clean room at INEEL. It is described in Ref. [10].

Radioactivity measurements of the purified enriched Mo powder samples using HPGe spectroscopy in the LSM show that the most stringent limits obtained for radiopurities are ^{214}Bi<0.2 mBq/kg and ^{208}Tl<0.05 mBq/kg. The required limit on ^{214}Bi (Eq. 2) is directly measurable. The task of measuring the required limits for ^{208}Tl (Eq. 3) is beyond the practical measuring limits of the HPGe detectors in the LSM. However, the chemical extraction factors defined as the ratio of contamination before and after purification were measured [10] for natural and enriched Mo. With evidence implied by Ra extraction limits and indirectly inferred by measurable quantities of ^{235}U in the enriched Mo samples, there is strong evidence that the ^{208}Tl contamination will be below the NEMO 3 design criteria. Ultimately, the NEMO 3 detector will measure these activities.

The chemically purified ^{100}Mo is used to make composite foils in the method previously discussed. There are two types of backing film used, Type 1 for sector 1 and Type 2 for sectors 05 and 10 through 16.

To produce the composite strips, the first step is a sieving of the powder to keep only grains with diameter smaller than 45 μm. Then, the residual is ground up and there are additional sieving processes because the grains have to be small enough to ensure a good bond. Next the powder is mixed with the glue (water and PVA). The mixture is introduced into a syringe, which is heated with ultra-sound to obtain a paste, of which the chosen thickness is uniformly spread onto one of the two Mylar foils (backing film). Finally the paste is covered with the second backing film. After 10 hours of drying, the composite strip is ready with a length of around 2500 mm, a width of 63 or 65 mm and a surface density lower than 60 mg/cm^2.

After the radioactivity measurement (see Table 3 for best limits) as with the metallic foils, a group of seven composite strips is installed in a frame to produce a source foil, which is then introduced into the sector. The total mass of ^{100}Mo in composite foils is (4435 ± 22) g.

2.1.6 Production, enrichment and purification process for others isotopes

- **^{82}Se source**

There is also a high enough mass of ^{82}Se to study the $\beta\beta0\nu$ process. One can use a similar enrichment process to that used for Mo, but here one produces a $^{82}SeF_6$ gas.

Two different production runs of 500 g for Se were carried out. They had an enrichment factor of 97.02% for run 1 and 96.82% for run 2. No subsequent purification process was carried out. A portion of run 1 was already used in the NEMO 2-prototype and a value for the ^{214}Bi contamination was measured, but the contaminants were found to be concentrated in small "hot spots" and rejected in the analysis via identification of the vertex of the candidate events [11]. The ^{82}Se used in NEMO 2 foils was recovered and used to produce composite strips for NEMO 3. The sample of material from run 2 plus the remaining part of run 1 were also used to produce composite strips. Low activities in ^{214}Bi ((1.2 ± 0.5) mBq/kg) and ^{208}Tl ((0.4 ± 0.1) mBq/kg) were measured in 0.8 kg of ^{82}Se strips with the HPGe detector, as shown in Table 3 (the NEMO 3 required limits for selenium are given in Eq. 4 and 5). These correspond to an expected background of 0.2 events/yr/kg from ^{214}Bi and 1 event/yr/kg from ^{208}Tl, but it is expected that the measured contamination in these Se foils may again be localized and will be suppressed through data analysis. In the mean time a purification process is being developed at INEEL for potential future runs with several kilograms of Se.

Se enriched powder was used to make composite strips at ITEP, with Type 3 backing film in sectors 06 and 07, and Type 1 in sector 08. The total mass of ^{82}Se is (932 ± 5) g.

- **^{130}Te source**

There are two different experimental measurements of the $\beta\beta2\nu$ half-life for ^{130}Te [12], [13], which are unconsistent with each other. For this reason, it was decided to study $\beta\beta2\nu$ with NEMO 3.

Te is enriched (89.4% of isotope 130) by the production of $^{130}TeF_6$ gas, but this time followed by oxidation and reduction to obtain enriched TeO_2 powder. The reason for TeO_2 versus Te is that it is easier to work with. The Kurchatov Institute (Moscow, Russia) provided the powder to the NEMO collaboration after three separate purifications. For this sample radioactivity limits for ^{214}Bi and ^{208}Tl were measured but also a small contamination of ^{228}Ac (^{232}Th decay chain) was detected suggesting that the limit on ^{208}Tl is close to a value which NEMO 3 should measure (see Table 3). Composite strips were made with Type 1 backing film. A total mass of 454 g of ^{130}Te was placed in sectors 09 and 17.

- **^{116}Cd source**

Metallic enriched cadmium ((93.2 ± 0.2) % of isotope 116) is obtained by the centrifuged separation method. Part of the sample had been measured with the NEMO 2 prototype [14]. Another part was purified by a distillation technique.

Despite the metallic quality of the cadmium source, strips were glued between Mylar foils to provide mechanical strength in the vertical position. A total mass of (405 ± 1) g of ^{116}Cd was placed in sector 18.

- **^{150}Nd source**

$^{150}Nd_2O_3$ powder was provided by INR (Moscow, Russia), after enrichment (90.97% of isotope 150) by electromagnetic separation and chemical purification. Radioactivity measurements (see Table 3) showed ^{214}Bi < 3.0 mBq/kg (maximum level of contamination required for NEMO 3 is 83 mBq/kg) but there was a small contamination of ^{208}Tl ((10 ± 2) mBq/kg instead of $<$ 5.5 mBq/kg for NEMO 3). As a consequence, this source will be used to check the ability of NEMO 3 to measure internal background.

The one neodymium composite strip (number 6 of sector 05) is made with 40.18 g of enriched Nd_2O_3 powder and backing films of Type 1. This gives a total mass of 37 g of ^{150}Nd.

- **^{96}Zr source**

Enriched zirconium was obtained by an electromagnetic separation technique, with 57.3% of ^{96}Zr. The result was a powder of $^{96}ZrO_2$, from two different origins.

The first sample came from ITEP and was measured in the NEMO 2 prototype. The contamination of ^{40}K, ^{228}Ac and ^{208}Tl was measured. As with the Se the contaminants were concentrated in “hot-spots” and removed in data analysis [15]. The $^{96}ZrO_2$ powder was recovered from NEMO 2 foils and purified using a chemical process. It represents 9.58 g of ZrO_2 or 4.10 g of ^{96}Zr. The second sample comes from INR (Moscow, Russia) and is 12.42 g of ZrO_2 or 5.31 g of ^{96}Zr.

The zirconium composite strips were made with enriched ZrO_2 powder, backing films of Type 2 and constitute the 7th foil in sector 05. The total mass of ^{96}Zr is approximately 9.4 g.

- **^{48}Ca source**

$CaCO_3$ enriched in isotope 48 of calcium ($(73.17 \pm 1.6)\%$) was produced by electromagnetic separation methods in Russia. Additionally, a purification process was developed collaboratively by JINR and the Kurchatov Institute. It removes ^{226}Ra, ^{228}Ra, ^{60}Co and ^{152}Eu, as well as elements from uranium and thorium decay chains. The obtained purification factors for $^{226(228)}$Ra, ^{60}Co and ^{152}Eu are greater than 1300, 3300 and 250 respectively. After the purification process, with 64 g of enriched $CaCO_3$, JINR had a yield of 42.064 g of enriched CaF_2 powder.

A first portion (24.558 g of enriched CaF_2) of this powder was used for radioactivity measurements with HPGe studies in the LSM. Only limits have been obtained (see Table 3).

The second portion of this powder (17.506 g) has been used to make nine 40 mm diameter disks. Mylar was again used and cut in the shape of the disks to form a sandwich. To create the calcium strip (about 25% of the 7th foil in sector 05), the sandwiches were glued between two Type 2 backing films. There is about 7 g of ^{48}Ca.

- **^{nat}Te and copper sources**

Foils of $^{nat}TeO_2$ inserted into the detector allows one to measure the external background for ^{100}Mo. The effective Z of these foils ($Z(^{nat}TeO_2) = 43.2$) is nearly the same as that of the molybdenum foils (Z(Mo)$=$ 42). This is useful because the external γ-ray background can give rise to contamination processes, which are all proportional to Z^2. Thus, the background for ^{100}Mo and $^{nat}TeO_2$ foils should give rise to similar event rates. In addition, although $^{nat}TeO_2$ has 33.8% ^{130}Te, the $\beta\beta2\nu$ process expected has $Q_{\beta\beta} = 2.53$ MeV and so these events would not enter the signal region of ^{100}Mo. Thus, a background subtraction is possible for ^{100}Mo foils using analysis of the $^{nat}TeO_2$ spectrum.

It is also useful to study $\beta\beta$ processes for the ^{130}Te part of $^{nat}TeO_2$ (33.8%) compared to enriched TeO_2. Foils of $^{nat}TeO_2$ were not purified but radioactivity measurements showed limits lower than 0.17 and 0.09 mBq/kg for ^{214}Bi and ^{208}Tl respectively, as shown in Table 3 (semi-conductor purity level).

The $^{nat}TeO_2$ composite strips were made with Type 1 backing films for 5 strips in sector 08 and Type 3 for the 7 strips in sector 19. This gives a total mass of 614 g of $^{nat}TeO_2$ or 208 g of ^{130}Te.

The copper foil provides a similar study of external background to $^{nat}TeO_2$ foils for a smaller value of Z. The metallic copper source is very pure (^{214}Bi $<$ 0.12 mBq/kg and ^{208}Tl $<$ 0.04 mBq/kg) and a mass of 621 g is placed in sector 00.

2.2 Design of the calorimeter

2.2.1 Description

The three functions of the NEMO 3 calorimeter are to measure the particle energy, make time-of-flight measurements and give a fast trigger signal. The calorimeter is constructed with 1940 counters, each of which is made with a scintillator, light guide and PMT (3" or 5"). The gains of the PMTs have been adjusted to cover energies up to 12 MeV. The plastic scintillators were chosen to minimize backscattering and for their radiopurity. The scintillators completely cover the two cylindrical walls which surround the tracking volume. There is also partial covering of the top and bottom endcaps, or *petals*.

The scintillator blocks share an interface with the helium-alcohol gas mixture of the tracking detector in order to minimize energy loss in the detection of electrons. The blocks are supported by a rigid frame, which allows the PMTs to be outside the helium environment. This configuration prevents rapid aging of the PMTs due to the helium.

The nomenclature for the calorimeter scintillator arrays is shown in Fig. 2. Note that the arrays of scintillator for the calorimeter's endcaps are identified as L1 through L4 as one goes out radially. For the cylindrical walls of a sector the internal wall uses the designation IN for the array and for the external wall there are EC and EE arrays to distinguish the blocks in the center (EC) versus the edge (EE) of the wall. The scintillator thickness (10 cm) has been chosen in order to obtain a high efficiency (50%) for γ-ray detection (500 keV) so as to measure the residual radioactivity of the source foil and also to reject background events.

2.2.2 Scintillator and light guide characteristics

The INR Kiev-Kharkov collaboration (Ukraine) was given the charge of producing the 480 endcap scintillators and JINR was assigned the 1460 wall scintillators. The scintillator is a polystyrene-based plastic combined with a scintillating agent p-Terphenyl (PTP) and a wavelength shifter (POPOP). The proportions of polystyrene, PTP and POPOP are respectively 98.49, 1.5 and 0.01% for endcaps scintillators and 98.75, 1.2 and 0.05% for the blocks of the walls.

As performance inspections, the energy resolution $\frac{\sigma(E)}{E}$ for 1 MeV electrons had to be better than 6.2%. This resolution was checked during construction using 482 and 976 keV conversion electrons produced by a ^{207}Bi source. After etching the blocks under water to obtain diffusive reflection at the surfaces, there was an improvement in the resolution by about 1%. The average values of the energy resolution were respectively 5.1% for IN blocks and 5.5% for EE and EC blocks. To ensure the use of scintillators with the best resolution, a greater number of scintillator blocks were produced: 1093 IN blocks for 680 used (62%), 994 EE blocks for 520 used (52%) and 428 EC blocks for 260 used (61%).

Scintillator blocks were then sent to CENBG and IReS for positioning blocks with the best resolution on the walls and on the petals of the detector respectively.

The radiopurity of both types of scintillator was measured. The scintillator was found to be 430 and 60 times lower in activity for ^{214}Bi and ^{208}Tl than the PMTs used to read it out, which are also low radioactivity PMTs (see Table 4).

For the light guide PMMA (polymethacrylate) plexiglas was produced for the experiment and used for the scintillator and PMT interface, which then protects the PMTs from helium. The light transmission through the guides is 98% in the wavelength range 380-420 nm. To ensure rigidity the light guide is glued to an iron ring, which provides a pressfit between the guide and the petal or wall.

2.2.3 Photomultiplier tube characteristics

Development of low background PMTs was begun in 1992, in a collaboration between different manufacturers and physicists studying dark matter and neutrino oscillations. The selection criterion for the low radioactivity glass was for the contamination in ^{40}K, ^{214}Bi and ^{208}Tl to be lower than 1.7, 0.83 and 0.17 Bq/kg respectively. The Hamamatsu company was chosen to produce the PMTs for NEMO 3, with the radiopurity of their glass being 100 to 1000 times better than standard glass (see Table 4). The other parts of their PMTs also have very low contamination (see section 2.8 for the radioactivity measurements of the PMTs).

The IN, L1, L2 and L3 scintillator blocks were coupled to R6091 3" PMTs (230 g, 1040 pieces). These tubes have 12 dynodes and a flat photocathode. The EE, EC and L4 scintillator blocks were coupled to R6594 5" PMTs (385 g, 900 pieces). The tubes have 10 dynodes and a hemispherical photocathode for structural integrity and thus need a second interface guide to match the design between the PMT and the light guide.

The Hamamatsu PMTs were chosen not only for low background but also for their performance. A dedicated test station using a H_2 lamp was developed. The energy and time resolutions were measured at 1 MeV, the average values were respectively 9% and 250 ps. The linearity of the response of the PMT was studied as a function of the energies between 1 and 12 MeV. Also, the symmetry and the uniformity of the photocathode was investigated and finally the noise at the minimal threshold, 10 mV ($\sim$ 33 keV).

2.2.4 Preparation and installation of the scintillator blocks

Five layers of 70 μm thick Teflon ribbon were wrapped around the four lateral faces of scintillator block to diffusely scatter the scintillation light for improved light collection.

A visual check on the color of the block was made. The energy resolution and the peak position at 1 MeV are checked again for several locations on the entrance face of the block with an electron spectrometer using ^{90}Sr source. The spectrometer has an intrinsic energy resolution of 0.6%. This test identified and rejected blocks with inhomogeneities.

All six faces of the blocks, with the exception of the contact region for the light guide, were covered with sheets of aluminized Mylar. The Mylar not only protects the scintillators from ambient light but also from light produced by Geiger propagation plasma in the tracking region, while enhancing the light reflection inside the scintillator and minimizing energy lost by the electrons out of the entrance face.

After gluing [3] the scintillator block to the petals and the walls, the peak position and energy resolution at 1 MeV were measured at the center of each block, using the electron spectrometer. This information was used to identify particular scintillator block and PMT combinations so as to obtain an energy resolution for the calorimeter which is as uniform as possible. The performance of the calorimeter is given in section 3.4.

2.2.5 Assembly of the PMTs in the LSM

Once a sector was transported to the LSM, the 3" PMTs were glued directly to the light guides, while the 5" PMTs had the interface guide glued to the light guide. After a check to see that the system was light tight, the magnetic shield of μ-metal was placed around the PMTs.

[3] A systematic check of the radiopurity for all the glues used in the NEMO 3 detector was carried out in the LSM [16]

2.3 The tracking detector

The tracking volume of the NEMO 3 detector is made of layers of vertical drift cells working in Geiger mode. After a long period of research and development at LAL, which had the responsibility of the tracking detector, the optimal parameters were identified for the best resolution and efficiency while minimizing multiple scattering effects. This optimization involved a balance between two parameters which contribute to aging effects of the wires. The first is the diameter of the cell's wires which needs to be as low as possible for better transparency in the tracking device. The second is the proportion of helium and alcohol in the gas mixture.

2.3.1 Elementary Geiger cell

The cross section of each cell is "octogonal" in design with a diameter of 3 cm, consisting of a central anode wire surrounded by 9 or 10 ground wires. Instead of just 8 wires, there are additional wires to avoid electrostatic cross talk between cells of adjacent layers. All the wires are stainless steel and are 50 μm in diameter and 2.7 m long. The wires are strung between the two iron petals of each sector which form the top and bottom of the detector (seen in Fig. 2). On each end of the cell, there is a cylindrical cathode probe, which will be refered to as the cathode ring. The cathode ring is 3 cm in length and 2.3 cm in diameter. The anode wire runs through the center of this ring while the ground wires are supported just outside the ring. If one compares NEMO 3 to the previous prototypes NEMO 1 and NEMO 2, there is a new mechanism for securing the wires in the petals. The advantages of the new mechanism are that it allows for easy wire installation, avoids the radioactivity of solder, and provides easy removal in replacement is necessary.

The cells work in the Geiger mode with a mixture of helium gas with ethyl alcohol. The characteristic operating voltage for the anode wires is 1800 V. When a charged particle crosses a cell the ionized gas yields around 6 electrons per centimeter. These electrons drift towards the anode sense wire at a speed of about 2.3 cm/μs when the electrons are close to the anode; when they are far away from the anode wire the mean drift velocity is around 1 cm/μs, because the layout of the wires (field and ground) leads to a varying electric field within a cell.

Measurement of this drift time is used to reconstruct the transverse position of the particle in the cell. The Geiger regime has a fast rise time for the anode pulse (around 10 ns) which can be used with a fixed threshold to provide a good time reference for the TDC measurements (see paragraph 2.4). In the Geiger regime, the avalanche near the anode wire develops into a Geiger plasma which propagates along the wire at a speed of 6 to 7 cm/μs, depending on the working point (Geiger plateau) which is a function of the gas mixture and operating voltage. The arrival of the plasma at the ends of the wire is detected with the cathode rings mentioned above. The propagation times are used to determine the longitudinal position of the particle as it passes through the cell.

2.3.2 NEMO 3 tracking device

Tracking simulations in a 30 Gauss magnetic field were investigated. The study revealed the optimum configuration for the layers of cells in the sectors of NEMO 3. Taking into account multiple scattering in the track reconstruction the result was 4 layers near the source foil followed by a gap, then 2 layers and another gap followed by 3 layers near the scintillator wall (the "4-2-3" layer configuration). Thus, there are 9 layers on each side of the source foil and possibly 9 track measurements. The gaps between the groups of cell layers is due to the position of the plastic scintillators on the petal. The 4 layers near the source foil are sufficient to provide a precise vertex position. Two layers in the middle and three layers close to the plastic scintillator walls provide good trajectory curvature measurements. Each pair of adjacent cells in a given layer has two grounded wires in common which allows for tight packing.

2.3.3 Assembly and wiring of a sector

To suspend the wire cells the iron petals have an intricate pattern of holes drilled into them in order to support the 4-2-3 layer configuration. The sectors are wired in a class 10,000 clean room. Studies with prototypes have confirmed the need for very high quality wire for proper plasma propagation. To fulfill such requirement a special production of 200 km long and 50 μm in diameter stainless steel wire was contracted [4], with a precision on the diameter better than 1%. Wires are strung layer by layer, alternating ground and anode wires. The wiring of one sector takes about four weeks for 1991 wires.

Cells are of high quality if two conditions are satisfied simultaneously: at operating voltage the counting rate is free of secondary triggers and electrical discharges while having the Geiger plasma propagate to both extremities of the cell. A special box of 6.4 m^3 was used to test each of the 20 sectors. The measured counting rates in the cells using cosmic rays is around 60 Hz compared to 2 Hz in the LSM before the coil and shields were added. Thus a test for one week corresponds to several years of operation in the LSM. As a result of the anode tests, on average 10 of the 340 anode wires were replaced

[4] Trakus factory, Germany

per sector. Fewer than 10 ground wires per sector were replaced. This exercise also demonstrated the efficiency of cell repair.

The final step, to ensure a tight seal to contain the helium, uses silicon RTV to outline the regions to be sealed, and then Araldite. Gas tightness is also ensured between petals and walls, at the exterior of the sector.

2.4 Electronics, trigger and data acquisition systems

The NEMO 3 detector is composed of two electronically logical parts. The first is the calorimeter and the second is the tracking detector with Geiger cells. There are independent electronics and data acquisition systems for the two with a trigger system that can be dependent on both. The electronics, trigger and data acquisition are separated into modules which share a VME bus. This design permits not only $\beta\beta$ runs, but also different tests to adjust and calibrate the detector.

2.4.1 Calorimeter electronics

The PMT bases are designed with a tapered voltage divider to improve the linearity under conditions of high current. Tests carried out at the IReS laboratory identified fixed sets of resistors for the PMT bases which control the voltage between the photocathode and the first dynode so as to optimize the time resolution.

Three large power supplies from CAEN [5] are used to supply the HV for the 1940 PMTs. Each HV channel is shared by 3 PMTs via a distribution board. The 3 PMTs must be similar in gain and fine tuning is done with two variable resistors on the distribution board for each PMT. Data taken with a ^{207}Bi source was used to set the PMTs' gains. There are nine distribution boards per sector and each board has 4 HV channels that in turn supply 12 PMTs.

The 97 PMTs of each sector are divided by the source foil into the interior and exterior regions. A total of 46 PMTs are used for the interior region of which 6 PMTs are on the top and bottom petals. The exterior region is covered with 51 PMTs, again with 6 PMTs are on the top and bottom petals. Thus there is a total of 40 half-sectors for which front-end electronics boards are designed. The corresponding 40 mother boards are housed in 3 VMEbus crates and each mother board supports 46 or 51 analog-NEMO (ANEMO) daughter boards.

[5] CAEN HV power supply type SY527 10 boards A938 AP, 24 channels each, with AMP multicontact connectors

The ANEMO boards have both a high and a low threshold discriminator. If the PMT signal exceeds the lower level threshold it starts a TDC measurement and opens a charge integration gate for 80 ns. The high threshold discriminator is adjustable up to 1 V but generally runs at 48 mV corresponding to 150 keV. The high threshold discriminator works as a single shot that delivers an event signal to the mother board.

Each mother board in turn provides an analog signal to the trigger logic which reflects the number of channels that have exceeded the upper threshold. The signal strength is 1 mA per channel. This level is used to trigger the system (1st level trigger) if the desired multiplicity of active PMTs is achieved. The trigger logic then produces a signal called *STOP-PMT*, which is sent to all the calorimeter electronic channels, to save their data. So the TDCs are stopped and the charge integration is stored. Then digital conversions begin. At the same time, a signal is sent to the calorimeter acquisition processor, which permits the read out of the digitized times and charges for the active channels.

The analog-to-digital conversions of the charge and the timing signal are made with two 14-bit ADCs of which only 12 bits are used. The energy resolution is 0.36 pC/channel ($\sim$ 3 keV/channel) and the time resolution is 53 ps/channel.

If the PMT signal exceeds the lower level threshold but not the high level threshold then the TDC measurement and charge integration are aborted and the system resets after 200 ns.

2.4.2 Tracking detector electronics

The Geiger electronics are divided into two types of boards. The first is a secondary voltage distribution which provides 1800 V to the anode wires. Included on the secondary distribution boards are the analog signals from the anode wire and the two cathode rings. These boards receive high voltage from two of the CAEN power supplies [6]. The second type of board for the tracking electronics is an acquisition board which is connected to the distribution board. It uses ASICs [7] and an interface part with a 50 MHz clock (20 ns per channel).

The functions of the acquisition board are first amplification and then discrimination of analog signals coming from the distribution board. Time measurements for each cell are acquired for the anode wire and the two cathode times. Note that the two cathode times are identified as t_{LC} and t_{HC} where LC and HC stand for low and high cathode times. The low one corresponds to the cathode ring on the bottom of the detector and the high one is for the top of the detector.

[6] CAEN HV power supply type SY527 with A734P boards, 16 channels each
[7] Application Specific Integrated Circuit

Each of the 20 sectors need the following electronics. Eight secondary distribution boards, each of which receives 5 daughter boards for the anode, low cathode and high cathode signals. Each daughter board corresponds to 8 cells, so that there are 40 cells per distribution board. Next each sector needs 8 acquisition boards, which receive 10 analog ASIC and 10 digital ASIC, with each ASIC handling 4 cells, which again services 40 cells per board.

Each of the 4 channels of the analog ASIC[8] is used to amplify the anode and cathode signals by a factor of 60, and to compare them to anode and cathode thresholds generated by a software programable 8-bit DAC. For signals exceeding the thresholds, a comparator provides a TTL signal which is sent to the TDC scalers of the digital ASIC. There are 4 TDCs for each of the 4 channels of the digital ASIC[9]. The first three are for the anode tdc_A, low cathode tdc_{LC} and high cathode tdc_{HC} contents which are measured with a 12-bit TDC and give times between 0 and 82 μs. The alpha TDC, tdc_α, is a 17-bit one, which provides time measurements between 0 and 2.6 ms.

The anode signal starts the TDCs and creates an OR signal (called *HIT*) for all the cells of a layer for a given sector; that means 360 TTL signals are sent to the T2 trigger.

The propagation of the Geiger plasma is detected by pick-up electrodes (cathode rings) at the extremities of the Geiger cells. These signals stop their respective cathode TDCs and give tdc_{LC} and tdc_{HC} values. Physical propagation times are proportional to these values:

$$t_{LC} = [tdc_{LC} \times 20]\,\mathrm{ns} \tag{6}$$

$$t_{HC} = [(tdc_{HC} \times 20) - 17.5]\,\mathrm{ns} \tag{7}$$

The time constant, 17.5 ns, is removed from t_{HC} to take into account the length difference between low cathode cable (6 m) and high cathode cable (9.5 m).

Concerning the anode signal, there are two cases which have to be distinguished. The anode signal can exceed its threshold before or after the arrival of the *STOP-A* signal which comes from the trigger (see Section 2.4.3). In the first case, for β-type events, the *STOP-A* signal is used to stop tdc_A channels which have received an earlier start signal. Anode times t_A, correspond to the transverse drift time by:

$$t_A = [(tdc_{max} - tdc_A) \times 20]\,\mathrm{ns} \tag{8}$$

[8] 1.20 micron technology from AMS inside PLCC 44 boxes
[9] 1.00 micron technology from ES2 inside PLCC 68 boxes

where $tdc_{max} = 307$. The maximum time is 6.14 μs and is measured from tdc_A spectra.

In the second case, for α-type events, all Geiger cells not already triggered can register delayed hits which occur after the *STOP-A* has been received for up to 710 μs. Anode signals exceeding their threshold start not only anode and cathode TDCs but also alpha TDCs (tdc_α).

Cathode signals stop the cathode TDCs and give tdc_{LC} and tdc_{HC} values, but the anode and alpha TDCs are stopped by the *STOP-α* signal coming from the trigger. As a consequence, in this case the tdc_A and tdc_α have the same value modulo 4096 for these cells. The corresponding alpha time t_α is then given by:

$$t_\alpha = [(tdc_{\alpha\_max} - tdc_\alpha) \times 20]\,\mathrm{ns} \qquad (9)$$

where $tdc_{\alpha\_max} = 35430$, which corresponds to $\sim$ 710 μs. This value is measured from the alpha TDC spectra.

2.4.3 The NEMO 3 trigger system

The trigger system was developed by LPC. The trigger system receives one analog signal from each of the 40 half-sectors that is proportional to the number of PMTs that have exceeded their high threshold in that sector. That signal is summed with the other 39 half-sectors resulting in an analog signal, which reflects the multiplicity of active PMTs throughout the detector. The trigger then goes onto the second level which involves the Geiger layers. In this case there are 360 channels of binary information to be used. The 360 channels are generated by treating each Geiger layer in each sector as a bit, which is on if the layer is hit. This enables the use of a rough track recognition program to be run on the available Geiger cell information. It is then possible to refine the identified tracks by spatially connecting the Geiger cells and fired PMTs.

Timing constraints and trigger strategy have lead to a three level trigger system (see Fig. 4).

The **first level (T1)** of the trigger, is embedded on the T1-3 board, and is based on the number of PMTs required to initiate a readout. It is used to identify the number of active scintillators by using the summed current from the 40 analog signals to define the multiplity of the event *(MULT)*.

If the trigger logic encounters a multiplicity higher than that set by the *MULT* threshold up to 20 ns after the first triggered PMT, the T1 configuration generates the *STOP-PMT* signal, which is the timing reference of the experiment, with a precision better than 150 ps.

The **second level (T2)** consists of track recognition in the Geiger layers, using the 40 half-sectors. The track recognition is first performed on a per half-sector basis. Nevertheless, the probability for an electron to cross more than one sector is high, so tracks that cross two adjacent half-sectors are searched for in a second step. Thus, there are two secondary levels:

- The first one is a search between 4 different possible tracking patterns, which correspond respectively to a long track, a short track near the foil, a short track near the scintillator block or no track;

- The second one consists of making special associations between adjacent half-sectors. For example a long track in a half-sector and any kind of track or no track in the adjacent half-sector. Another possibility is to use two short tracks in two adjacent half-sectors, one near the foil and the other near the counter, which permits the trigger to select a full track contained in more than one sector.

This level is embedded on the T2I (internal) and T2E (external) boards, which receive 180 *HIT* signals each and provide 9 logical signals coming from a logical OR which lasts for 1.5 μs on the cells of each layer. If the trigger logic is satisfied for the chosen track condition, a second level local trigger is generated.

From the hardware point of view, one has to program the T2 level conditions into the T2I/E boards via a set of programmable memories.

The **third and last level (T3)** is embedded on the T1-3 board and checks on the possible coincidence between pre-tracks from T2's second step and fired *PMT* half-sectors. This level is only used for calibration runs, to select precise electron tracks coming from radioactive sources installed in the calibration tubes. It is implemented in hardware without the possibility of changing the algorithm. For the case of *PMT+GG* trigger conditions, if the second level trigger is detected:

- the *STOP-A* signal is sent to Geiger acquisition boards with a programmable delay, set to 6.14 μs after the *STOP-PMT* signal;

- two trigger signals are sent respectively to Geiger and calorimeter electronics with a programmable delay set to 6.14 μs after the *STOP-PMT* signal. The first one stops the automatic time-out which occurs 102 μs after the *STOP-A*. The second permits the digitization of the analog signals of the activated PMTs. In case these signals are not received there is an automatic and individual reset of PMT channels, which have started measurements.

- the *STOP-α* is sent to Geiger acquisition boards with a fixed delay of 710 μs after the *STOP-PMT* signal.

2.4.4 The NEMO 3 data acquisition system

The control and readout of the calorimeter and Geiger cell crates is performed with the inter-crate VICbus by two CES RIO 8062 computer modules equipped with PowerPC 604E-300MHz CPU chips. The data acquisition system is based on Cascade operating under a Lynx-OS software package developed at CERN [17]. It uses two boards: Corbo PMT for the calorimeter readout trigger and Corbo GG for the track detector readout trigger. The two independant acquisition processors for the calorimeter and the Geiger collect PMT and Geiger cell information in parallel. After the processors have read out the event and de-activated their "busy" signal, the trigger system reinitializes its logic electronics for the next event. Data buffers for the calorimeter and Geiger cells are then sent to the event builder processor (EVB) via the PVIC bus (multidrop PCI-to-PCI high speed link), as described in section 3.2.

2.4.5 Survey of the experiment

A monitoring and survey system of the experiment was installed on two dedicated PCs in the LSM. It permits local or remote control of several systems and operating parameters such as electric boxes; crates, boards and channels for distribution, acquisition and HV; pressure and temperature of the wire chamber gas system; current to the magnetic coil... It is also used for the ON/OFF high-voltage procedure for the Geiger cells and the calorimeter.

2.4.6 The NEMO 3 database: NEMO DB

The MySQL database management system is used for NEMO 3. Data synchronization in the *NEMO DB* server network is based on the replication concept of the MySQL package. Here any number of servers can be tuned to replicate and transfer data from one primary server. The structure of the NEMO MySQL servers includes the primary server at the LSM in Modane for the information stored in the on-line database, the main server at Lyon CCIN2P3 containing all the information, and a set of local servers (mirrors of the main server).

The *NEMO DB* contains the electronic logbook of the runs, the calibration parameters of scintillator counters and of Geiger cells, as well as information about the run conditions.

2.5 Energy and Time calibration of the counters

2.5.1 Introduction

In order to measure a precise value of the absolute energy released in a double beta decay ($Q_{\beta\beta}$), an appropriate calibration procedure needs to be established. The chosen solution for NEMO 3 is to use radioactive sources decoupled from the detector and present only during runs dedicated to calibration. These absolute energy measurements, which need long data taking, will take place only 2 or 3 times a year. Thus, daily control of the stability of the counters has to be done additionally with a survey system using a laser.

Timing information is used to discriminate between external and internal events for background studies (see paragraph 1.3). The relative timing offsets for each of the 1940 counters has to be determined, using particles emitted in coincidence from a radioactive source. Particle times of flight have also to be corrected for several effects, as the amplitude corrections due to leading edge discriminators (called time-energy corrections), or TDC slope corrections. It is also done using the laser survey system.

2.5.2 Mechanics of the calibration tubes

Each of the 20 sectors of the detector is equipped with a vertical flat tube located along the edge of the source foils (see Fig. 2) and 3 pairs of kapton windows: one window of the pair is oriented towards the internal wall and the other towards the external one. The size of the windows ($\sim 500\ \mathrm{mm}^2$) and their vertical positions ($z = -90,\ 0$ and $+90$ cm) have been chosen to obtain an approximately uniform illumination of the scintillator blocks by 3 radioactive sources placed inside the tube. The source carrier is a long narrow delrin tongue supporting 3 removable source holders. Introduced into the copper tube from the top of the detector, after removal of a plug fitted into the shield, this carrier allows each of the 3 sources to be positioned between a couple of windows, their location being known with a precision better than 1 mm in all directions.

2.5.3 Radioactive sources

For energy calibration of the counters, one needs radioactive sources which emit electrons. The choice was made to use ^{207}Bi and ^{90}Sr sources. Decay of the first one provides conversion electrons of 482 and 976 keV energy (K lines) suited for a calibration in the region up to about 1.5 MeV. The product of ^{207}Bi decay is essentially γ-rays, thus the tracking chamber must be in operation to select electrons originating directly from one of the sources. To measure energies up to 3 MeV or more, one needs at least one additional calibration point, which is obtained using electrons from ^{90}Y (daughter of ^{90}Sr) and measuring the end point of the β spectrum at 2.283 MeV. This calibration doesn't require pattern recognition because the events of interest are located in the tail of the spectrum, which can only contain electrons coming directly from the sources. It allows the use of intense sources and thus a higher speed for the event collection.

For time calibration, the relative timing offsets for each channel are determined with a ^{60}Co source, emitting 2 coincident γ-rays with respective energies 1332 and 1173 keV. Spectra of arrival time differences are collected to establish time delays between the 1940 channels. This time calibration doesn't require the use of the tracking chamber and allows the use of intense sources.

2.5.4 Laser calibration system

In an experiment such as NEMO 3, which requires stability for many years over a large number of PMTs, frequent tests of the detector's stability are of paramount importance. The objectives of the chosen laser calibration system [10], as shown in Fig. 5, are first a daily check of the absolute energy and time calibration, which permits the calculation of the corrections according to the laser peak position, then the measurement of the PMTs linearity between 0 and 12 MeV and finally the determination of the time-energy relation. To accomplish this, the laser light must be known with very high accuracy ($< 1\%$) and must be stable during the measurement; one needs a precise calibration of the optical filter transmission for the energy range 0 to 12 MeV and a good common time reference (STOP); the shape of the laser signal has to be identical to the one produced by an electron.

The N_2 laser wavelength of 337 ± 15 nm is selected. Then the light beam is separated into 2 parts. The first one is sent to a photodiode, which monitors the laser light intensity. A variable optical attenuator can be used to adjust the flux. The second part of the light goes through two filter wheels with different optical filters of known transmissions to simulate the full range of energy. This part of the laser light is then shifted (to 420 nm) and sent to 3" PMTs and 5" PMTs respectively by means of optical fibers. The shifter is a scintillator ball, wrapped in Teflon and aluminum to increase diffusive reflections, which mimics electron signals created in the NEMO 3 scintillators. Six reference counters, which are equipped with ^{207}Bi sources, permit the control of the laser light by measuring energies of both laser light and 976 keV conversion electrons emitted from ^{207}Bi. Each optical fiber [11] is divided in two parts and the distance between these two parts is adjustable using individual

[10] MNL 202 laser from Lasertechnik Berlin; 200 kW, 10 Hz
[11] Toray PFU-CD501-10-E

attenuators, which permit the distribution of the same quantity of light to each of the 1946 counters.

The daily laser procedure is carried out in two steps: the first one, during the $\beta\beta$ run, consists of laser heating and parameter checking, photodiode pedestal measurement and laser light measurement (and flux correction if necessary); the second step is made at the end of the $\beta\beta$ run. It consists of a pedestal measurement for the 1946 PMTs, then a rotation of the two filter wheels (to obtain a 1 MeV equivalent flux), followed by the acquisition of laser light (1946 PMTs) and ^{207}Bi (6 PMTs) events. Finally the laser is stopped and the filter wheels are moved to the opaque setting in order to prevent light being inadvertantly sent to the NEMO 3 counters and a new $\beta\beta$ run is started. For the calibration up to 12 MeV, one repeats this procedure twice a year with different equivalent fluxes, changing for each run the rotation of the two optical attenuator disks for each run ("complete" laser run).

2.5.5 Absolute energy calibration method

In the full range of energies measured by NEMO 3 (up to 12 MeV) the relation between electric charge signal and deposited energy in the counter is not necessarily linear. Nevertheless, the relation is linear up to 4 MeV, where the best precision is required:

$$E = a\,(C - P) + b \tag{10}$$

where C is the ADC value of the associated scintillator and P is the pedestal. The energy calibration constants a and b are determined using at least two points from measurements with radioactive sources, while the "non-linear" relation is determined using a "complete" laser run.

The energy resolution is assumed to have essentially two contributions: a main component originating from the statistical fluctuations of the number of photoelectrons at the PMT anode which increases as the square root of the energy and a second component due to the instrumental effects being energy independent. These two terms contribute to the resolution in quadrature in the form:

$$\sigma(E) = \sqrt{A \times E} \oplus B \tag{11}$$

Using 60 ^{207}Bi sources of ($\sim$ 220 Bq each) with a high threshold of 48 mV ($\sim$ 150 keV), around 5000 events produced by scintillator hits associated with selected tracks are registered for each PMT. Then the positions of the two main peaks corresponding to 482 and 976 keV conversion electrons are extracted and the resolution is obtained as a result from the fit of the 976 keV peak position.

Using 4 ^{90}Sr sources ($\sim$ 6 kBq each) simultaneously, 8 runs are taken with these sources in different positions, with a threshold of 450 mV ($\sim$ 1.5 MeV). Between 500 and 1000 events are registered to form a spectrum for each PMT. A fit to the high-energy tail of the spectrum is made with a function describing the shape of a single β spectrum of ^{90}Sr, convoluted by the energy resolution function $\sigma(E)$ and taking into account the mean energy loss of the electrons.

Finally, these 3 results (2 peaks and end-point) from the calibration runs with ^{207}Bi and ^{90}Sr are combined to extract the parameters a and b of a straight calibration line valid in the energy region up to 4 MeV (measurements of the pedestals can be used in addition to give an extra constraint at the other end of the energy range). Results of energy calibrations are presented in section 3.4.

2.5.6 Energy corrections using the laser system

The laser procedure is carried out as a reference just after the calibration runs and gives E_0 for each counter (one assumes there is no correction to apply to the b offset). At a later time t a new value E_t is measured:

$$E_0 = a_0(C_0 - P_0) + b \qquad \text{and} \qquad E_t = a_t(C_t - P_t) + b = e_{corr} \times a_0(C_t - P_t) + b$$

where e_{corr} is the correction factor to apply. It represents the variation of the calibration slope of the counter between the reference time and t. This variation of the laser light is determined using two different methods. The first one compares the laser peak position (C_{laser}) and the 976 keV peak position from ^{207}Bi (C_{Bi}) between the reference time and t for the 6 reference PMTs; the second one uses a mean value of the laser peak position given by the NEMO 3 counters. These two results are compared to check their consistency, but only the first one is transferred to the database.

The "real" energy value $E_{(t)}^{(i)}$ for counter number i and at instant t is finally:

$$E_{(t)}^{(i)} = [(C_{(t)}^{(i)} - P_{(t)}^{(i)}) \times a^{(i)} \times e_{corr_{(t)}}^{(i)}] + b^{(i)} \qquad (12)$$

2.5.7 Time calibration

The timing response of two counters detecting two particles emitted in coincidence depends not only on the time-of-flight of each particle, but also on several effects which have to be corrected for.

- **Time alignment of the counters**

All PMTs must be aligned in time. The time taken for each PMT to respond to a signal depends on the individual characteristics of the PMT. In order to use only one time scale, an alignment procedure has been developed to obtain the individual time shifts $\varepsilon^{(i)}$ ($i = 1, 1940$) associated with each PMT. The procedure to find $\varepsilon^{(i)}$ uses γ-rays emitted in coincidence by the ^{60}Co radioactive source and detected by a pair of scintillators. There is a common *start* in the electronics for both counters due to the ^{60}Co decay mode and these electronics use a common *stop-pmt* for all the counters, which allows the individual delays to be extracted.

In order to calculate the time of flight correctly, only one ^{60}Co source of 15.5 kBq has to be used per run (10 runs with different source positions have to be performed in order to cover all possible combinations of PMT). With a threshold of 150 mV ($\sim$ 500 keV), spectra of arrival time differences are collected and the relative timing offset $\varepsilon^{(i)}$ for each counter i is determined (see Section 3.4).

• **Other corrections**

The effect of leading edge type discriminators is to induce a time-vs-energy dependence, which can be parameterized with a formula using four parameters

$$t(C) = p_1 - \frac{p_2}{p_3\sqrt{C} + p_4} \tag{13}$$

and takes into account physical effects responsible for the pulse shape. Determination of the parameters $p_k^{(i)}$ ($k = 1, 4$ for counter i) is accomplished through a "complete" laser run producing equivalent energies between 0 and 12 MeV. The relative timing offset $\varepsilon^{(i)}$ for counter i is then included in the asymptotic value $p_1^{(i)}$.

The laser survey system is also used to obtain daily time response corrections for each counter, which correspond to TDC slope variations: $t_{corr} = tdc_t - tdc_0$.

Finally, the "real" time $T_t^{(i)}$ used for time-of-flight calculation, for counter number i and at instant t is:

$$T_{(t)}^{(i)} = tdc_{(t)}^{(i)} - t_{corr_{(t)}}^{(i)} - t(C_{(t)}^{(i)}) \tag{14}$$

2.6 Coil and shields

2.6.1 Introduction

To reach design sensitivity for the effective neutrino mass, there must be no events (< 0.1) from external background in the energy range [2.8-3.2] MeV during the planned five years of data taking of NEMO 3. The external background contribution coming from neutrons is due to (α, n) reactions, spontaneous fission of uranium and the interaction of cosmic ray muons in the rocks. The γ-ray flux in the LSM has been studied using a NaI detector surrounded by different shields [18].

As shown in paragraph 2.8, the detector has been designed with stringent radiopurity selection criterion for its construction materials. For the external background contribution coming from γ-rays and neutrons, several studies with the NEMO 2 detector as well as the NEMO 3 simulation [19], have shown that large reduction on these backgrounds are achieved by the use of a solenoid capable of producing a field of 25 G, surrounded by two external shields, the first one to reduce γ-ray and thermal neutron fluxes, the second to suppress the contribution of slow and fast neutrons. The design of the coil and of the shields allows the dismounting of the elements to access each sector of the detector.

2.6.2 The magnetic coil

The simulation of the fast neutrons coming from within the laboratory into NEMO 3 was carried out with 20 cm of iron shield. The contribution to the $\beta\beta0\nu$ background by the photons created by neutron capture leads mainly to (e^+e^-) events and also to a few (e^-e^-) produced in the source foils. The detection by the calorimeter of the γ-rays associated with these events provides a high rejection efficiency (80%). A 25 G magnetic field, which provides the charge determination of the charged particles in using its trajectory curvature, permits the rejection of 95% of the (e^+e^-) pair events.

The coil surrounds the entire detector and so access to the detector was a necessary design consideration. Thus, the coil is made of 10 sectors with 203 copper rings connected from one sector to the next one, with only one layer (see Fig. 1). The finished coil part is cylindrical, 5320 mm in diameter, 2713 mm in height and a mass of 5 tons (~ 3.1 tons of selected copper).

2.6.3 Iron shield

The iron shield, which surrounds the NEMO 3 detector and the coil, is made of ten parts (165 tons) with two endcaps (6 tons each) in addition, the lower one is fixed and the upper one is mobile. The thickness of this iron shield is 20 cm, except for few parts where it is 18 cm on account of its position. The iron was selected for its radiopurity, as shown in Table 6.

2.6.4 Neutron shield

The remaining (e^+e^-) pair events (5% not rejected by curvature) and the (e^-e^-) events due to the photons created by neutron capture can be suppressed only if the flux of neutrons inside the detector is decreased. A neutron shield optimized to stop fast neutrons with an energy of a few MeV, which also suppresses thermal and epithermal neutrons is used.

The neutron shield is made of three parts, as shown in Fig. 1. The first one is situated below the central tower of the detector (not shown in the figure) and consists of 20 cm thick paraffin. The second part covers the endcaps below and above the detector, and consists of 28 cm of wood. The walls are covered with 10 large tanks containing borated water, 35 cm thick, separated by wood of 28 cm thickness.

2.7 Mounting and assembly of the detector in the LSM

2.7.1 Metallic framework

The steel framework, which supports the NEMO 3 sectors, is made of two parts. It was installed in the LSM at the end of 1998 and supports the 20 sectors of the detector, the 10 parts of the magnetic coil and of the shields, as well as the strand of cables. All the components of the framework were selected for their radiopurity. All the electronics racks containing the calorimeter and the tracking detector boards, as well as the trigger and acquisition boards, are arranged under this framework.

2.7.2 Placing of the sectors on the metallic frame

Once the sectors had been made helium tight, anode and cathode cables were connected to each sector, which was then transported to the LSM, where the mounting of the PMTs was carried out. After gluing and testing of the PMTs, the sector was carried inside the enclosed frame with surpression system and cleaned using alcohol and nitrogen gas.

The source frame, which supports the seven foils of each sector, was prepared simultaneously in the clean room. The source frame was then mounted in the enclosed frame to be introduced inside the sector. Finally, the calibration tube was set in position, the sector was cleaned again with nitrogen and then closed with Mylar foils.

The enclosed frame was then opened to move the sectors, which are hung on the metallic framework. The calorimeter cables (HV and signal) were soldered to the PMT bases and to the boards, once the distribution daughter boards for the tracking detector were installed on their mother boards. These operations were followed by the introduction of the plastic optical fibers into a brass tube which is present in each light guide of the calorimeter. Finally, all the connections were tested for the calorimeter, the tracking detector and the laser system (both electrical and optical). During these operations, each sector was filled with nitrogen.

All the operations (construction of the sectors, installation on the metallic frame, helium integrity, filling of the sectors with helium and alcohol, triggering and acquisition) have been checked since April 2000 for three sectors (00, 18 and 19). During the same period, the 17 other sectors of NEMO 3 were installed, the last one in August 2001. Then, the 20 sectors were placed in their definitive positions and the helium tightness of the detector was made using RTV glue.

The total fiducial volume inside the tracking detector is 28 m^3 (excluding the scintillator volume). The filling of the detector with gas was done in December 2001, using a fast flushing of helium gas (5 volumes), followed by injection of ethyl alcohol in the gas regulation system. The whole process took around 24 h. A constant pressure of gas was maintained with a flux of the order of 130 l/h until November 2002. The magnetic coil was installed in February 2002 and γ shield in April 2002. Finally, the installation of the neutron shield took place in February 2003. Between each step, $\beta\beta$ and calibration runs were taken to monitor stability and for input to simulations.

Data taking was stopped in December 2002 to make several improvements:

- changes in HT power supply for the calorimeter part to enhance PMT safety;

- improvement of the working of some noisy PMTs or PMTs with too low or too high gain;

- improvement of the helium tightness of the detector;

- addition of argon in the gas mixture of the tracking detector (with V(Ar)/V(He) = 1%), in order to improve Geiger cell stability and efficiency of longitudinal propagation of the cells and also to limit the aging problems. At the same time, the proportion of quencher in the mixture was reduced from 40 to 39 mbars partial pressure (that means ethyl alcohol at 14^{o}C instead of 15^{o}C).

In mid-February 2003, new $\beta\beta$ runs commenced in optimal conditions, with coil and both shields.

2.8 Radiopurity of the detector

2.8.1 Introduction

As described in paragraph 1.3, for energy deposits in the range of a few MeV as is the case in double beta decay experiments, radionucleide concentration has to be as low as possible in the materials used in the detector construction. In order to minimize internal background the sources have to be purified, whereas to minimize external background it is necessary to have low background PMTs. Radioactivity in ^{208}Tl, ^{214}Bi and ^{40}K must also be controlled for all detector materials.

2.8.2 Measurement principle

Measurements of γ-ray spectra have been made using low background HPGe detectors located in the CENBG or in the LSM (in order to suppress any effect of cosmic rays). With a 400 cm^3 HPGe spectrometer, it is possible to use the "Marinelli" geometry, which consists of placing a large quantity of the substance in question around the HPGe crystal. The abundance of selected isotopes in the decay chain is determined by the strength of certain selected gamma lines, as measured with the HPGe detector.

2.8.3 Radioactivity measurements of the source foils

A 400 cm^3 HPGe spectrometer in the LSM has a sensitivity of 0.2 mBq/kg of ^{214}Bi and 0.06 mBq/kg of ^{208}Tl, with a 1 kg of the substance to measure in 1 month. Maximal allowed levels of ^{214}Bi and ^{208}Tl contamination in Mo sources are given in Eq. 2 and 3. The level of sensitivity necessary for ^{214}Bi is achieved but not for ^{208}Tl. The solution would be to count for more than one month but the collaboration have decided to make a compromise between the source measurement and the detector construction. Radioactivity measurements for all the NEMO 3 sources are summarized in Table 3. Only the best ^{100}Mo measurements are presented, for both metallic and composite strips. In this table it can be seen that for ^{208}Tl only limits have been obtained except in ^{82}Se and $^{150}Nd_2O_3$ strips. In the case of ^{82}Se, the presence of "hot-spots", which can be suppressed by analysis, is suspected. For ^{150}Nd, note that the $Q_{\beta\beta}$ value (3367.1 keV) is well above the 2615 keV γ-ray produced in the decay of ^{208}Tl.

2.8.4 Radioactivity measurements for the other components of NEMO 3

As explained in paragraph 2.2.3, the Hamamatsu company was chosen to produce low background PMTs, with very low contamination of all their components (glass, insulator, ceramics, etc). In NEMO 3 the total mass of the PMTs is 239.2 kg of 3” and 346.5 kg of 5” PMTs, which lead to the total activities presented in Table 4.

After selection of the PMTs, the other materials (except shields) were chosen if their total activities in ^{40}K, ^{214}Bi and ^{208}Tl were at most one tenth of the total activities for PMTs. It is not always possible to satisfy this criterion for the three contaminants: if there is a higher contamination only in ^{40}K, the material is nevertheless accepted because ^{214}Bi and ^{208}Tl produce more background events in the $Q_{\beta\beta}$ region. In Table 5 the measurements for all selected components of a 5” PMT are summarized . The two last lines of this table allow the comparison of the activity of the selected materials and the total activity of the PMT, the first one being at most the same order as the second. Thus these materials were used to build the calorimeter.

Finally, to conclude on the NEMO 3 radiopurity, a summary of the radioactivity measurements is given in Table 6 for the main components of the detector.

3 Performance of the detector

3.1 The simulation program

The NEMO 3 simulation program [20] has been developed in the framework of GEANT [21], with the EUCLID industrial software and the EUCLID-GEANT interface [22] for the description of the NEMO 3 device (geometric information, description of 40 materials and 16 tracking media) with 20 identical sectors, except for the source foils which can be placed in any desired position in the detector.

The event generator of the program, called *GENBB*, provides the possibility of generating all possible double beta decays (0ν, 2ν, Majorons) for the NEMO 3 nuclei. Also internal and external background events due to decay of radioactive nuclei may be generated. This event generator also provides the possibility of generating the kinematics of special events, such as Compton scattering of external γ-rays or Möller scattering of external electrons, thereby speeding up the computations compared to the simulation of these events by GEANT itself.

Important work has been done on the simulation of neutron interactions, performed with the GEANT/MICAP code [23], which allows the tracking of neutrons from 20 MeV to 10^{-5} eV. This code takes into account γ-ray emission, from (n,γ) captures and (n,n'γ) scatterings. Using results of several tests done with the NEMO 2 detector [19], the γ-ray generation subroutines were improved by including additional spectroscopic information related to nuclei and a new library, GAMLIB, was developed taking into account branching ratios down to as low as0.1%. Additionally, MICAP was modified to allow for the emission of conversion electrons, which is particularly important for neutron captures with the large internal conversion coefficients observed in many nuclei. A comparison between the simulation and the data with a Am-Be neutron source, using the magnetic field and no shield, is presented in Fig. 6 and shows the excellent agreement for high energy crossing electron events e_{cross} (with $E_e > 3.2$ MeV).

In Table 7, the experimental number of ($e_{cross}N\gamma$) events (with $N \geq 0$) observed per hour is compared to the expected number of events from simulation. This simulation takes into account γ-ray flux from the laboratory as well as thermal, epithermal and fast neutron fluxes, for which the respective proportions are given in this table. It was supposed that the epithermal neutron flux was equal to the thermal one. The resulting number of observed events is (2.19 ± 0.17) to compare to (2.05 ± 0.25) simulated events per hour. The agreement is still very good with the gamma shield (attenuation factors are shown in Table 7), which provides a global experimental attenuation factor of 3.2 ± 0.4, with $\sim$ 1200 rejection factor for γ-rays and $\sim$ 100 for thermal neutrons. The number of associated two electron background events due to neutron flux, with the γ shield, is (13.6 ± 4.4) for the two electrons' energy greater than 2.75 MeV; however, the experiment requires that there be no external background. Finally, the addition of the neutron shield, which provides a global attenuation factor of $\sim$ 70 according to the simulation, will suppress this background.

3.2 Trigger and data acquisition

3.2.1 Acquisition and data file building

Data transfer is achieved via private Ethernet connection. The Event Builder processor *EVB* (400 MHz, with Powerful Ethernet controller) sends data event by event to a PC running under Linux. In the transfer, Linux processes the data and it is decoded and re-organized into Random Access ZEBRA files: the initial format of Cascade events uses a 12-word header, followed by calorimeter and Geiger information with variable length (2 words per triggered PMT and 3 words per fired cell), and finally a 3-word trailer; the final format is an "ntuple" format for data analysis. The ntuple building is done on the acquisition local disc and the zebra file is written every 5000 events.

3.2.2 Trigger type properties

• **The $\beta\beta$ trigger configuration**

For $\beta\beta$ runs, the trigger configuration (see section 2.4.3) is a two level one, which enables the readout detection of events with at least one electron or electron-gamma event. This configuration has the following properties:

- at least one triggered scintillator with energy deposited greater than 150 keV;

- track building in a half-sector or two adjacent half-sectors, with two possible configurations corresponding to the activation of Geiger cells in at least 3 of the 9 layers, with at least two fired cells in neighbouring layers (using either at least 2 out of the 4 layers near the source foil, or the two intermediate layers, or at least 2 out of the 3 layers near the scintillator wall).

The associated counting rate is (7.4 ± 0.1) Hz.

The $\beta\beta$ trigger efficiency was estimated by applying trigger criteria to simulated signal and background events with at least one fired Geiger plane and at least one fired PMT ($\beta\beta0\nu$ or $\beta\beta2\nu$ events from ^{100}Mo sources, ^{214}Bi and ^{208}Tl background events from ^{100}Mo sources, and ^{214}Bi decays from gas). The number of generated events for each type is 10000. Results are summarized in Table 8, both for events with at least one fired PMT or at least two fired PMTs. The proportion of accepted simulated events are given in the first (respectively third) column for at least one (respectively two) PMT(s). The lost is mainly due to geometrical cuts. The proportion of accepted events after applying trigger criteria are given in second and fourth column: it represents the trigger efficiency. It has been shown from this study that trigger criteria do not provide additionnal cuts and allow to keep for further analysis all interesting events. The trigger efficiency relative to the number of events with exactly two fired PMTs (criterium for $\beta\beta$ analysis) are respectively 100% for $\beta\beta$ events (both 0ν and 2ν), 96.7% and 94% for Bi and Tl in sources and 74.5% for Bi in gas.

In the usual trigger conditions of $\beta\beta$ runs, dead time is due both to the 710 μs delay devoted to the measurement of alpha particles and to the Geiger readout dead time, which is at least 587.5 μs for 3 triggered Geiger cells. For each event the Geiger processor reads the 160 Geiger acquisition cards' status bits and 5 counters for each fired cell; through VICbus a single read cycle needs about 2.5 μs; finally interrupt handling and Cascade overhead take around 150 μs. Thus for a $\beta\beta$ event with 2 triggered PMTs and an average of 16 triggered

Geiger cells, the global dead time is (710+750) μs, around 1.5 ms.

• **Other acquisition types**

With the same trigger configuration, one can have higher counting rates and lower dead times using acquisitions without delayed events: it is impossible to remove the 710 μs fixed delay, but the Geiger readout can begin on the calorimeter interrupt. In this case the busy Geiger and the busy calorimeter are superimposed and the overlap is reduced to about 200 μs, which give a global dead time of $\sim$ 1 ms.

It is possible to take data with just the calorimeter (600 Hz) of just the tracking detector. For laser runs, the counting rate is 250Hz, with 10Hz/PMT of that being the laser data, and the remainder coming from 207Bi in the 6 reference PMTs.

Calibration runs with 60 ^{207}Bi sources use a $\beta\beta$ trigger, with an acquisition rate of $\sim$ 240 Hz. Other source types use only calorimeter acquisition, with a special one developed for ^{90}Sr: to determine the beta end-point, the acquisition of only the energy spectra is realized without ntuple building for all the calorimeter, which permits very high counting rates (up to 30 kHz) with smaller hbook files of 32 Mbytes (all the 32 Mbytes of the calorimeter processor are allowed for histograms).

Counting rates associated with different trigger and acquisition types are presented in Table 9.

3.2.3 Proportion of events in a $\beta\beta$ run

The combination of a tracking volume, delayed tracking electronics, calorimetry and a magnetic field allow NEMO 3 to identify electrons, positrons, γ-rays and delayed-α particles.

- electron (positron): one e^- (e^+) is reconstructed as a track, defined by hits in time, with negative (positive) curvature starting from the source foil, passing through the wire chamber and being detected by only one scintillator (because electrons and positrons have a low probability to emit bremmstrahlung γ-rays, which could trigger neighbouring scintillators).
- alpha particle from the source foil: one α-particle is reconstructed as at least one delayed hit near an electron or a positron vertex, or as a short straight track defined with delayed hits within 1.5 μs and passing through the wire chamber.
- gamma: a γ-ray corresponds to one or two adjacent scintillators being triggered, without any associated track and without single Geiger hit in front of the scintillator. If there are two scintillators in the cluster, they must

have been simultaneously triggered, with their time difference lower than the sum of their temporal resolutions.

Fig. 7 shows a typical two electron event coming from a molybdenum source foil ($\beta\beta 2\nu$ process). In Fig. 8, 9, 10 and 11 one can see events characteristic of some contamination associated with the detector: $e^-\gamma\gamma\gamma$ event, e^+e^- pair production, $e^-\alpha$ event and high energy crossing electron.

The proportion of different types of events in a $\beta\beta$ run is given in Table 10. Note that $\beta\beta$-like events represent 0.15% of the registered events, that means one $\beta\beta$-like event every 1.5 minute.

3.3 Tracking detector performance

3.3.1 Final operating conditions of the tracking detector

The gas mixture used for normal running is He+Ar (with $V(Ar)/V(He) =$ 1%) + ethyl alcohol as the quencher (39 mbars partial pressure) at a flux of 300 l/h. An overpressure of $\sim$ 10 mbars is maintained to ensure against contaminants entering the gas volume. The longitudinal propagation velocity is 5.2 cm/μs corresponding to a full propagation time $< t_{LC} + t_{HC} >\sim 50$ μs and 90% of Geiger cells have a longitudinal propagation efficiency > 95%. The single counting rate per cell is $\sim$ 0.2 Hz.

There were eventually 30 dead channels (< 0.5%) because of a missing anode signal: 4 cells are disconnected due to anode wire in contact with ground inside the detector, 8 cells due to interconnection problems, and 18 hot cells ($\sim$ 0.3%) were temporary disconnected. The number of Geiger cells with a missing cathode signal = 160 (1.3%), due to interconnection problems.

3.3.2 Geiger TDC analysis

As discussed in section 2.4 four variables corresponding to the Geiger TDC contents are called respectively tdc_{LC} and tdc_{HC} for the two cathode times, tdc_A for the anode time and tdc_α for the delayed time (see Eq. 6 to Eq. 9). The Geiger hits are classified into different types, according to the values of these four TDC contents:

- hit in time (used in track reconstruction);

- delayed hit (candidate for delayed-α track reconstruction);

- refired hit, fired by a neighbouring in-time hit (1-2 per event rejected);

- noisy hit (negligible proportion rejected).

These criteria will be explained in more detail below.

3.3.3 Track reconstruction

• Principle

Geiger hits are first selected depending on the status of the four previously defined criteria. Then, two different pattern recognition and fit procedures are carried out, one for hits in time, and the other for delayed hits.

Hits in time: pattern recognition and tracking are carried out using a cellular automaton algorithm, which was already used for NEMO 2 tracking [24]. The principle of the NEMO 3 algorithm is described here: using a set of consecutive segments connecting each pair of fired cells in neighbouring layers, a candidate track is defined and characterized by a number of segments (length of the track) and the sum of the angles between its segments. In NEMO 3, the longest track is favored during a quality test. Concerning the curvature of the track, the criterion depends on whether there is a magnetic field or not. Then one suppresses all segments used for the track and a new track search can begin with the other segments, until there are not enough segments remaining to reconstruct a track.

Concerning the track fitting procedure, there are two successive fits in order to solve left/right ambiguities in the transverse plane.

Each track reconstructed in time is extrapolated onto the foil plane and a vertex position is calculated, whose transverse and longitudinal coordinates are in $R\phi$ and Z. In the same way, the track is projected onto the associated scintillator surface and the calculated coordinates at the scintillator are $R\phi_S$ and Z_S.

Delayed hits: the treatment in z is the same as for hits in time. The treatment in the transverse plane is slightly modified since there is only a relative drift time measurement. Delayed hits can be associated only if the difference in anode time between the hits is lower than 1.5 microseconds, which is approximately the maximal drift time in a Geiger cell. For each hit, the drift distance is computed from the tdc_α content of the cell, supposing the delayed hit with the higher tdc_α content correspond to a particle passing through the anode wire of the cell. To improve the vertex reconstruction of the delayed track, a second iteration of the fit is done, using the information from the reconstructed vertices from the in-time tracks, which are less than 4 cm in $r_\perp$ and in z from the reconstructed vertex of the delayed track after the first iteration of the fit (it is supposed here that delayed tracks and ordinary tracks have a common vertex, which corresponds to $e^-\alpha$ or $e^+\alpha$ events).

- **Association between tracks and energy deposits in calorimeters**

To define electron or positron events, one needs to associate a track with a scintillator, which is done if at least one hit in the two nearest Geiger layers to the scintillators belongs to the track. Moreover, geometrical cuts are applied: the extrapolated position of the track at the entrance surface of the scintillator ($R\phi_S$ and Z_S) has to be located less than 5 cm away from the center of the scintillator block.

3.3.4 Reconstruction of the particle position in the cell

Studies with a laser and a 9 cell prototype of the tracking detector were first carried out to establish formulae giving transverse ($r_\perp$) and longitudinal (z) positions in a cell (respectively from anode drift time and from both cathode times). Then, these formulae were improved with the full running detector [25], using data taken with high energy crossing electrons (> 4.5 MeV). These electrons were created by an intense Am-Be source producing fast neutrons with an activity around 2.2 10^5 n/s. Fast neutrons are thermalized in scintillators; high energy γ-rays are created by the capture of neutrons in the copper walls; one crossing-electron events are then produced by the Compton effect. With high energy crossing electrons (with an energy deposited > 3 MeV for the second triggered scintillator), the multiple scattering is negligible for the track fit.

Using these high energy crossing electrons, the track resulting from the fit is assumed to be identical to the real track. Thus transverse and longitudinal reconstruction formulae are obtained by comparing the distance to the fitted track with the drift anode time and the two cathode times.

- **Transverse position in the cell**

Fig. 12 shows the transverse distance $r_\perp$ to the fitted track as a function of the anode time t_A. Near the wire (between 1 and 4.5 mm), the drift velocity corresponds to the saturation regime and its value is 2.3 cm/μs. Far from the anode wire, the drift speed is proportional to the electric field. Thus, for $220 < t_A < 1480$ ns, the electric field is proportional to $1/r$, which leads to a transversal distance proportional to $\sqrt{t_A}$.

- **Longitudinal position in the cell**

According to the two measured cathode times t_{LC} and t_{HC} and using the origin of the z axis fixed at the vertical center of the cells, the longitudinal position z is given, in mm, by:

$$z = \frac{L_{eff}}{2} \frac{t_{HC} - t_{LC}}{t_{LC} + t_{HC}} \left[1 - 0.505\ 10^{-4} \frac{L_{eff}}{2} \left(1 - \left|\frac{t_{HC} - t_{LC}}{t_{LC} + t_{HC}}\right|\right)\right]$$

where $L_{eff} = 2607$ mm is the effective length of the cell, lower than the full cell length of 2700 mm (including the two rings of 30 mm long). This effective length is the consequence of the fact that cathode signals exceed their electronic threshold a few centimeters before the plasma comes inside the cathode ring. L_{eff} depends on HV and gas mixing.

The first order term corresponds to a constant propagation speed for the plasma. In this case, the longitudinal position is simply the propagation time of the plasma to the nearest ring, divided by the propagation velocity.

The second order term is a correction, which takes into account the decrease of the propagation velocity due to a decrease of the high voltage during the plasma propagation (this factor also depends on HV and gas mixing). The correction has a maximal value of around 20 mm in two positions corresponding respectively to 0.25 and 0.75 of the cell length.

If one of the two cathode times is missing, the relation remains the same, but only for the tdc with a non-zero value. The other cathode time is obtained using an average plasma propagation velocity for the plasma. The z position of the Geiger hit is then reconstructed using the same formula as above. The propagation velocity has to be calculated and stored in the Geiger database for each Geiger cell.

If both cathode times are missing, no reconstruction of the z position of the Geiger hit is possible.

- **Transverse and longitudinal resolution of the Geiger cells [25]**

The residual distribution in the transverse direction is obtained by plotting the distance between the fitted track and the reconstructed position of the Geiger hit, using high energy crossing electrons. The full width half maximum of the spectrum (FWHM) is used to compute the transverse resolution of the cells as $\sigma_\perp = FWHM/2.35$. The average value of this resolution is

$$\sigma_\perp = 0.5 \text{ mm}$$

Note that $\sigma_\perp/R \sim 3\%$, where R is the radius of the cell, with a value of 15 mm. In order to estimate the contribution of multiple scattering, a study of the transverse resolution was carried out as a function of the variable $\sqrt{L_{track}}/E$, where L_{track} is the track length and E is the initial energy of the electron in keV (see Fig. 13). The associated relation, which shows the resolution dependance with multiple scattering, is:

$$\sigma_{\perp} = \sqrt{\sigma_{int}^2 + k(\frac{\sqrt{L_{track}}}{E})^2}$$

where the intrinsic resolution is given by $\sigma_{int} = (0.37 \pm 0.02)$ mm and $k = (10.8 \pm 1.7)$ mm.keV^2 is a constant.

The longitudinal resolution of the cells is obtained with the same method applied in the longitudinal plane and the average value is

$$\sigma_{//} = 0.8 \text{ cm}$$

Note that $\sigma_{//}/L_{cell} \sim 3\%$, where L_{cell} is the length of the cell, with a value of 270 cm. Fig. 14 shows the influence of the zenith angle θ on the longitudinal resolution. $\sigma_{//}$ is multiplied by a factor of 2 for an electron crossing the wire with an angle $\theta = 45^o$ compared to a track perpendicular to the wire. It is due to the longitudinal spread of the primary ionization electrons along the anode wire. Fig. 15 shows the longitudinal resolution $\sigma_{//}$ as a function of the longitudinal position z. The associated relation is:

$$\sigma_{//} = \sigma_0 \times \sqrt{1 - (\frac{z}{L_{eff}/2})^2}$$

where $\sigma_0 = (1.050 \pm 0.008)$ cm is the maximal resolution at the center of the detector; L_{eff} is the effective length as already defined. This form is characteristic of the statistical fluctuations of the number of avalanches occuring during the longitudinal propagation.

3.3.5 Confusion between electrons and positrons [25]

Confusion between electrons and positrons has been studied with high energy crossing electrons produced by a neutron source, with an energy greater than 3 MeV. These events are reconstructed as two successive negative curvature electron-type events: the first one from one scintillator to the source foil on the first side of the foil, the second one from the source foil to a scintillator in the other side, both with a common vertex on the foil. Thus it is possible to check the probability of confusing a positive curvature positron-like event with an electron event after the foil. The associated distribution of the rate of error as a function of the electron energy is presented in Fig. 16. The e^+e^- confusion is around 3% at 1 MeV using extrapolated results.

3.3.6 The vertex reconstruction [25]

- **Principle**

Vertex reconstruction quality has been analyzed by taking data with 60 ^{207}Bi sources placed in the three positions (T for Top with $Z = 90$ cm, C for Center with $Z = 0$ cm, and B for Bottom with $Z = -90$ cm) on each sector inside the calibration tubes. The $R\phi$ and Z positions of these sources are known with an accuracy of 1 mm. ϕ is the polar angle, using cylindrical coordinates, with an origin at sector 0; $R = 155.5$ cm is the transversal distance between detector center and source foil; for sector 0, $R\phi = (148.6 \pm 0.1)$ cm for the three calibration sources and there is a step of 18 degrees to obtain $R\phi$ for each adjacent sector.

Conversion electron events coming from these sources are selected, with an energy of 482 keV or 976 keV. The distribution of the 60 reconstructed vertices are presented in Fig. 17. With this sample of data the differences between reconstructed and expected vertex positions can be estimated. The difference in the transverse plane is defined as $\Delta R\phi = R\phi_{\rm rec} - R\phi_{\rm exp}$ and in the longitudinal plane as $\Delta Z = Z_{\rm rec} - Z_{\rm exp}$.

For transverse reconstruction of the vertex, the differences are the same on average for the three source positions (T, C and B):

$$\Delta R\phi = 1.6 \text{ mm}$$

These small differences are compatible with the accuracy of $R\phi$ positions and with the tranverse resolution $\sigma_{R\phi}$ of the vertex (see next paragraph).

The average differences in the longitudinal reconstuction for the three positions are the following:

$$\Delta Z(T) = (-0.325 \pm 0.003) \text{ cm} \quad ; \quad \Delta Z(C) = (-0.164 \pm 0.007) \text{ cm}$$

$$\Delta Z(B) = (-0.052 \pm 0.003) \text{ cm}$$

Note the maximal value of this difference is lower than the longitudinal vertex resolution. The longitudinal position of the vertex is angle independent (for both θ and ϕ). However, an asymmetry for the three positions is observed, which corresponds to an error of around 20 ns on the cathode time measurement. It can be explained by the fact that the same discrimination threshold was used for both cathode signals although the high cathode signal is lower than the low one.

- **Vertex resolution**

The **transverse resolution** $\sigma_{R\phi}$ only depends on the energy of the track. Using the two conversion electron energy values (~ 0.5 MeV and ~ 1 MeV), it is possible to determine the average values for this resolution:

$$\sigma_{R\phi}(0.5 \text{ MeV}) = 0.3 \text{ cm} \quad \text{and} \quad \sigma_{R\phi}(1 \text{ MeV}) = 0.2 \text{ cm}$$

The **longitudinal resolution** σ_Z depends on both energy and position: using 1 MeV electrons, the same value $\sigma_Z = 0.7$ cm for both T and B positions is measured and a greater one, $\sigma_Z = 0.9$ cm is obtained for the central position. For 0.5 MeV electrons, the longitudinal resolution is $\sigma_Z = 1.1$ cm on average for T and B positions.

There is another dependence on the zenith angle θ (see Fig. 18), following the relation:

$$\sigma_Z = \frac{\sigma'_0}{\cos\theta}$$

where, on average, $\sigma'_0 = (0.632 \pm 0.004)$ cm for the T position, $\sigma'_0 = (0.825 \pm 0.006)$ cm for the central one and $\sigma'_0 = (0.615 \pm 0.004)$ cm for the bottom one.

• **Study with two electrons events**

For $\beta\beta$ analysis, it is necessary to reconstruct events with two tracks coming from the same vertex. Thus, it is important to study the vertex resolution of the two electron channel in order to check the measured transverse and longitudinal dispersions: $\delta R\phi$ and δZ are defined as the distance between the vertices associated with the two reconstructed tracks.

Using events coming from the 60 ^{207}Bi sources with two simultaneous electrons (intensity of $\sim 2\%$), it is possible to build $\delta R\phi$ and δZ distributions, which produce the associated resolutions:

$$\sigma(\delta R\phi) = 0.6 \text{ cm} \qquad \text{and} \qquad \sigma(\delta Z) = 1.0 \text{ cm}$$

Note that $\sigma(\delta R\phi) = 0.1$ cm, if one constrains the two tracks to have a common vertex.

These resolutions allow the distinction between two strips of the same source foil in one sector, which is crucial for sectors composed with different sources.

3.4 Operating conditions of the calorimeter

3.4.1 Working performance of the calorimeter

The operating voltages of the PMTs are 1800 V for the 3" and 1350 V for the 5" PMTs. The single counting rate is ≈ 0.2 Hz/PMT above a 48 mV high threshold (corresponding to an energy of ~ 150 keV). In total, 2% of the PMTs were not functioning to specifications.

3.4.2 Energy resolution of the counters

• **Energy calibration results**

As explained in paragraph 2.5, special calibration data are used to obtain three points on the energy versus ADC channel line: two resulting from multi-gaussian fits (K, L, M electrons) of the peak positions on the ^{207}Bi data, respectively at 482 and 976 keV (see Fig. 19), and one from the beta end-point at 2.283 MeV, which is obtained from ^{90}Sr data (see Fig. 20).

On average, the calibration line obtained from the two ^{207}Bi peaks as well as the fit combining ^{207}Bi and ^{90}Sr results, do not intersect the origin of the axes. This effect was already observed with data obtained with an electron spectrometer. A typical example, which represents the mean behavior of the counters, is given in Fig. 21.

It was first discovered with calibration data that the response of a counter depends upon the impact point of the electron, with a weak dependence of 1-2% for counters equipped with 3" PMTs and a stronger dependence of up to 10% for those equipped with 5" PMTs. This effect has a non-negligible consequence on the energy resolution, thus one has to correct it for the 7 types of counters, L1 to L4 for petal scintillators and EE, EC and IN for wall scintillators (see Table 11). One can see that these resolutions depend mainly upon the type of PMT associated to the scintillator: in average 6.1% for 5" PMTs and 7.3% for 3" PMTs.

3.4.3 Timing resolution of the counters

• **Time alignment of the counters**

As explained in section 2.5, the relative timing offset $\varepsilon^{(i)}$ for each counter i is determined using different calibration sources, in order to provide the time alignment of the calorimeter: ^{60}Co sources are used for time alignment with gamma rays; ^{207}Bi sources and one crossing electron events produced by neutrons from an external source are used for time alignment with electrons.

The distribution of the arrival time difference in the counters before and after alignment is shown in Fig. 22. The distribution after alignment has a resulting RMS of $\sim$ 700 ps.

The time resolution as a function of electron energy from double beta decay candidates is shown in Fig. 23: the time resolution is around 200 ps for 1 MeV electrons.

• **Time-energy corrections**

The energy dependence of the timing signal is adjusted by a four parameter formula, as shown in Eq. 13. The first way to find this relation is to use a "complete" laser run. A second way is to use data taken with neutron calibration sources, which give one crossing electron events. The result is plotted in Fig. 24 for the different types of scintillators.

- **The time-of-flight (TOF) selection criterion**

To distinguish between one crossing electron (oce) events (from external background) and back-to-back $2e^-$ events (from the source foil), the same TOF rejection criterion is applied as in the NEMO 2 experiment [4]. It is based on the comparison of the measured TOF (ΔT_{meas}) with the calculated one, assuming first that a single electron crosses the detector ($(\Delta T_{cal})_{ext}$ for external hypothesis) and then that two electrons are emitted from the source foil ($(\Delta T_{cal})_{int}$ for internal hypothesis).

Fig. 25 represents $(\Delta T_{meas} - \Delta T_{cal})_{int}$ vs $(\Delta T_{meas} - \Delta T_{cal})_{ext}$ for 2 track events reconstructed in ^{100}Mo foils. The plot shows well-separated bumps. The $2e^-$ events coming from the source foil are centered around $(\Delta T_{meas} - \Delta T_{cal})_{int} \sim 0$ ns. The oce events have $(\Delta T_{meas} - \Delta T_{cal})_{ext} \sim 0$ ns.

3.4.4 Counter stability

For each counter, the laser corrections are calculated using the absolute calibration obtained with sources as a reference and the laser light spectra. These corrections take into account any eventual variation of the laser light, which is monitored by reference PMTs. The stability of these PMTs is ensured by the measurement of conversion electron spectra from ^{207}Bi sources put in the associated reference PMT.

A typical example of the long term (one month) survey for the energy correction parameter (e_{corr}) for one counter is shown in Fig. 26. This stable behaviour is followed by 90% of the counters with 5" PMTs and 96% with 3" PMTs, with gain variations of less than 2%. These corrections are stored in the database and used with the associated $\beta\beta$ runs to calculate the energies. Improvements to these results are expected with stable data taking.

4 Conclusion

The NEMO 3 detector is running in optimal conditions, with coil and both shields, since mid-February 2003. Figures 27 and 28 are presented as performance results of the detector. The first one shows the distribution of the experimental total energy sum measured with molybdenum sources (background substracted) compared to $\beta\beta 2\nu$ Monte-Carlo. It corresponds to 650 hours of data taking between mid-february and end of march 2003. The number of events is 13750, with a signal to background ratio of 40. The second one presents the experimental angular distribution for molybdenum sources and the same data compared to $\beta\beta 2\nu$ Monte-Carlo: it is obtained using the ability of the NEMO 3 detector to reconstruct the two electron tracks, thus to measure the angle between them.

Acknowledgements

The authors would like to thank the Fréjus Underground Laboratory staff for their technical assistance in building and running the experiment.

The portion of this work conducted in Russia was supported by INTAS grant number 00-00362.

References

[1] W. H. Furry, *Phys. Rev.* **56** (1939) 1184

[2] A. S. Barabash, *Czech. J. Phys.* **52** (2002) 567

[3] D. Dassié et al., NEMO collaboration, *Nucl. Instr. Meth.* **A309** (1991) 465

[4] R. Arnold et al., NEMO collaboration, *Nucl. Instr. Meth.* **A 354** (1995) 338

[5] NEMO collaboration, NEMO3 Proposal, LAL 94-29 (1994)

[6] G. Audi and A.H. Wapstra, *Nucl. Phys.* **A 595** (1995) 409

[7] *Table of Isotopes*, 8th edition, R.B. Firestone, V.S. Shirley Editor (1996)

[8] *Table of Radioactive Isotopes*, E. Browne and R.B. Firestone, V.S. Shirley Editor (1986)

[9] D. Dassié et al., NEMO collaboration, *Phys. Rev.* **D51** (1995) 2090

[10] R. Arnold et al., NEMO collaboration, *Nucl. Instr. Meth.* **A474** (2001) 93

[11] R. Arnold et al., NEMO collaboration, *Nucl. Phys.* **A 636** (1998) 209

[12] T. Bernatowicz et al., *Phys. Rev. Lett.* **69** (1992) 2341

[13] N.Takaoka, Y. Motomura, K.Nagao, *Phys. Rev.* **C 47** (1996) 1557

[14] R. Arnold et al., NEMO collaboration, *Z. Phys.* **C 72** (1996) 239

[15] R. Arnold et al., NEMO collaboration, *Nucl. Phys.* **A 658** (1999) 299

[16] J. Busto et al., *Nucl. Instr. Meth.* **A492** (2002) 35

[17] Y. Perrin et al., *CASCADE: Tool kit for the construction of distributed real time data acquisition systems*, Conference Records of RT 93, Vancouver (1993)

[18] H. Ohsumi et al., NEMO collaboration, *Nucl. Instr. Meth.* **A482** (2002) 832

[19] C. Marquet et al., NEMO collaboration, *Nucl. Instr. Meth.* **A457**(2001) 487

[20] R. Arnold and V.I. Tretyak, *The NEMO 3 simulation program: current status*, **CRN 97-01** (1997)

[21] *GEANT - Detector description and simulation tool*, CERN Program Library Long Writeup W5013, CERN (1994)

[22] *EUCLID 3*, version 1.1F, Matra Datavision (1994)

[23] C. Zeitnitz and T.A. Gabriel, *Nucl. Instr. Meth.* **A349** (1994) 106

[24] I. Kisel et al., NEMO collaboration, *Nucl. Instr. Meth.* **A387** (1997) 433

[25] A.I. Etienvre et al., NEMO collaboration, *Performances of the tracking detector of the NEMO 3 experiment*, 2003, to be published in *Nucl. Instr. Meth.*

Sector	Source	η (%)	M_1 (g)	M_2 (g)	M_3 (g)
00	7 s. ^{nat}Cu **(M)**	/	620.8	620.8	620.8 $^{\mathrm{nat}}$**Cu**
01	5 s. ^{enr}Mo **(M)**	95.14	424.21	423.22	401.76 ^{100}**Mo**
	2 s. ^{enr}Mo **(C)**	95.14	176.22	145.08	137.72 ^{100}**Mo**
02	7 s. ^{enr} Mo **(M)**	1 and 2 : 96.81	186.44	186.06	179.76 ^{100}**Mo**
		3 to 7 : 98.51	434.88	434.40	426.94 ^{100}**Mo**
03	7 s. ^{enr}Mo **(M)**	98.90	697.32	696.47	686.29 ^{100}**Mo**
04	7 s. ^{enr}Mo **(M)**	97.90	614.63	614.14	600.05 ^{100}**Mo**
05	2 s. ^{enr}Mo **(M)**	1 and 2 : 98.20	188.27	187.89	184.14 ^{100}**Mo**
	3 s. ^{enr}Mo **(C)**	3 : 96.66	109.22	90.07	86.89 ^{100}**Mo**
		4 : 98.20	108.76	90.16	88.34 ^{100}**Mo**
		5 : 95.80	87.00	70.85	67.73 ^{100}**Mo**
	1 s. $^{enr}Nd_2O_3$ **(C)**	6 : 90.97	56.68	40.18	36.55 ^{150}**Nd**
	1/2 s. $^{enr}ZrO_2$ **(C)**	57.3 ± 1.4	11.57	7.15	ITEP : 4.10 ^{96}**Zr**
	(2 parts)	57.3 ± 1.4	14.94	9.27	INR : 5.31 ^{96}**Zr**
	1/4 s. $^{enr}CaF_2$ **(C)**	73.1 ± 1.6	18.516	9.572	6.997 ^{48}**Ca**
	1/4 s. back. film				
06	7 s. $^{\mathrm{enr}}$Se **(C)**	97.02	455.67	385.31	373.80 ^{82}**Se**
07	7 s. $^{\mathrm{enr}}$Se **(C)**	96.82	535.04	460.65	446.03 ^{82}**Se**
08	2 s. $^{\mathrm{enr}}$Se **(C)**	1 : 96.95	73.58	63.24	61.31 ^{82}**Se**
		2 : 97.02	62.78	52.82	51.25 ^{82}**Se**
	5 s. $^{\mathrm{nat}}TeO_2$ **(C)**	3 to 7 : 33.80	346.44	236.49	79.93 ^{130}**Te**
09	7 s. $^{\mathrm{enr}}TeO_2$ **(C)**	89.40	380.86	255.77	228.61 ^{130}**Te**

Table 1

Characteristics of the source strips (s. means strip) for each of the first 10 NEMO 3 sectors: η is the enrichment factor for the isotopic; M_1, M_2 and M_3 are respectively the total mass of material in the useful volume, the mass of investigated **element** in the useful volume, and the mass of investigated **isotope** in the useful volume. **(M)** and **(C)** identify metallic and composite foils respectively.

Sector	Source	η (%)	M_1 (g)	M_2 (g)	M_3 (g)
10	7 s. ^{enr}Mo **(C)**	1 and 2 : 95.14	205.9	170.14	161.51 $^{100}\mathbf{Mo}$
		3 to 6 : 96.66	414.68	339.94	327.92 $^{100}\mathbf{Mo}$
		7 : 96.32	102.91	84.73	81.45 $^{100}\mathbf{Mo}$
11	7 s. ^{enr}Mo **(C)**	5 : 95.14	107.88	89.44	84.92 $^{100}\mathbf{Mo}$
		others : 96.66	614.12	503.73	485.93 $^{100}\mathbf{Mo}$
12	7 s. ^{enr}Mo **(C)**	95.14	728.25	601.59	571.89 $^{100}\mathbf{Mo}$
13	7 s. ^{enr}Mo **(C)**	2 and 4 : 98.95	213.73	177.74	175.46 $^{100}\mathbf{Mo}$
		others : 96.20	508.93	420.9	404.1 $^{100}\mathbf{Mo}$
14	7 s. ^{enr}Mo **(C)**	98.95	735.11	608.07	601.00 $^{100}\mathbf{Mo}$
15	7 s. ^{enr}Mo **(C)**	96.20	753.85	627.59	602.62 $^{100}\mathbf{Mo}$
16	7 s. ^{enr}Mo **(C)**	1, 2, 4, 7 : 95.14	391.64	318.97	302.79 $^{100}\mathbf{Mo}$
		3 and 5 : 96.20	217.74	181.23	174.0 $^{100}\mathbf{Mo}$
		6 : 95.30	102.35	84.49	80.34 $^{100}\mathbf{Mo}$
17	7 s. $^{enr}TeO_2$ **(C)**	89.4	375.52	252.01	225.29 $^{130}\mathbf{Te}$
18	7 s. ^{enr}Cd **(M)**	93.2 ± 0.2	491.18	434.42	404.89 $^{116}\mathbf{Cd}$
19	7 s. $^{nat}TeO_2$ **(C)**	33.8	547.18	377.36	127.55 $^{130}\mathbf{Te}$

Table 2

Characteristics of the source strips (s. means strip) for each of the last 10 NEMO 3 sectors: η is the enrichment factor for the isotopic; M_1, M_2 and M_3 are respectively the total mass of material in the useful volume, the mass of investigated **element** in the useful volume, and the mass of investigated **isotope** in the useful volume. **(M)** and **(C)** identify metallic and composite foils respectively.

Source sample Activity (mBq/kg)	Meas. mass (g)	Exp. (h)	^{40}K	^{235}U	^{238}U chain		^{232}Th chain	
					^{234}Th	^{214}Pb ^{214}Bi	^{228}Ac	^{208}Tl
^{100}Mo **(M)** **2479 g**	733	840	< 5	1.5 ± 0.3	< 15	< 0.39	< 0.5	< 0.11
^{100}Mo **(C)** **4435 g**	735	648	< 6	< 0.3	< 15	< 0.34	< 0.3	< 0.10
^{82}Se **(C)** **932 g**	800	628	55 ± 5	20.0 ± 0.7	< 18	1.2 ± 0.5	< 1	0.4 ± 0.1
	292	500	200 ± 20	8.5 ± 0.9	< 25	< 4.2	< 4	< 0.70
$^{130}TeO_2$ **(C)** **454 g of ^{130}Te**	633	666	< 8	< 0.5	< 20	< 0.67	1.7 ± 0.7	< 0.46
^{116}Cd ((**M**) + mylar) **405 g of ^{116}Cd**	257	778	< 13	< 0.5	< 12	< 1.5	< 2	< 0.5
	299	368	< 20	< 1	< 56	< 1.7	< 4	< 0.83
$^{150}Nd_2O_3$ **(C)** **37 g of ^{150}Nd**	58.2	458	< 70	< 1	< 66	< 3.0	20 ± 7	10 ± 2
$^{96}ZrO_2$ ITEP **(C)** **4.1 g of ^{96}Zr**	13.7	624	< 217	< 7	< 222	< 16	< 23	< 10
$^{96}ZrO_2$ INR **(C)** **5.3 g of ^{96}Zr**	16.6	456	583 ± 167	< 10	< 211	< 14	< 27	< 5.5
$^{48}CaF_2$ **(C)** **7.0 g of ^{48}Ca**	24.56	1590	< 50	< 2	< 15	< 4	< 6	< 2
$^{nat}TeO_2$ **(C)** **208 g of ^{130}Te**	620	700	8 ± 3	< 0.3	< 17	< 0.17	< 0.9	< 0.090
Cu **(M)** **621 g**	1656	853	< 8	< 0.2	< 5	< 0.12	< 0.4	< 0.040

Table 3

Radioactivity measurements for all the NEMO 3 source foils (in mBq/kg). The total enriched mass of each isotope put in the NEMO 3 detector is given in bold characters. The error bars are statistical uncertainties at the 1σ level while the limits are at the 2σ level. A systematic uncertainty of about 10% is associated with the Monte Carlo calculations for the HPGe detector efficiencies. For ^{100}Mo only "best" measurements for both metallic and composite strips are noted. In the case of $^{48}CaF_2$, results are for the powder.

Total activity in Bq	^{40}K	^{214}Bi	^{208}Tl
3" PMTs R6091 - 1040 pieces (230 g/PMT)	354	86	5.2
5" PMTs R6594 - 900 pieces (385 g/PMT)	477	216	12.6
Σ PMTs	831	302	17.8

Table 4
Total radioactivity, in Bq, for all NEMO 3 Hamamatsu photomultipliers.

Sample	Weight (kg)	^{40}K (mBq/kg)	^{214}Bi (mBq/kg)	^{208}Tl (mBq/kg)
Magnetic shield (1.5 mm in thickness)	1.385	< 20	< 2	< 2
PMMA (light guide + interface)	1.500	< 50	< 5	< 3
Virole (pure iron)	0.555	< 35	< 3	< 3
Light-protect mantle	0.191	< 80	< 17	< 12
PMT-Guide glue RTV 615	0.072	380 ± 100	< 40	< 7
Light-protect glue for PMT RTV 106	0.025	250 ± 70	< 20	< 7
Teflon ribbon (5 layers)	0.023	< 170	< 20	< 5
Guide-Virole glue Epotek 310	0.017	< 110	< 15	< 3
Isolated circuit FR2 for PMT divider	0.0105	320 ± 100	57 ± 8	10 ± 3
Light-protect glue RTV 116	0.006	< 830	< 45	< 4
Scintillator-Guide glue BC 600	0.004	< 235	< 42	< 7
Aluminized mylar	0.004	< 700	< 35	< 20
White RTV 160	0.003	370 ± 130	35 ± 10	< 4
Capacitor 3.3 nF - 2 kV (1 piece)	0.003	< 230	< 17	48 ± 5
Capacitor 22 nF - 250 V (4 pieces)	0.002	< 1300	< 80	< 55
Radiel soldering Sn(63%) Pb(37%)	0.002	< 400	< 50	< 30
CMS resistors (23 pieces)	$21\ 10^{-5}$	< 9200	1400 ± 500	< 600
Total activity of these components **in Bq/PMT**		< 0.25	< 0.028	< 0.016
Total activity for one Hamamatsu 5" PMT **in Bq/PMT**		0.53	0.24	0.014

Table 5
Radioactivity measurements for 5" PMT components (in mBq/kg) ; Total radioactivity of these components, compare to the total radioactivity for one PMT (in Bq/PMT).

Main component in NEMO 3	Weight in kg	Total radioactivity in Bq			
		^{40}K	^{214}Bi	^{208}Tl	^{60}Co
Photomultiplier Tubes	600	831	302	17.8	no measurement
Scintillator blocks	6400	< 102	< 1.2	< 0.6	< 3
Copper	25000	< 125	< 25	< 10	< 6
Iron petals	10000	< 50	< 6	< 8	17 ± 4
μ-metal PMT shield	2000	< 40	< 4	< 4	< 4
Tracking detector wires	1.7	$< 8\,10^{-3}$	$< 10^{-3}$	$< 6\,10^{-4}$	$< 10^{-2}$
Iron shield	180000	< 3000	< 400	< 300	< 600

Table 6
Total radioactivity (in Bq) for the main components of the NEMO 3 detector. PMT activities are lower than specification requirements. Moreover, except for iron shield, all activities are clearly lower than the PMT's ones.

Type of events	Simulated flux (x 10^{-6} s^{-1}cm^{-2})	$e_{cross}N\gamma$ events in 1 h ($N \geq 0$) ($E_e > 3.2$ MeV)	Rejection factor from γ shield
γ-rays from lab.	3.2 ± 0.9	0.20 ± 0.05	1176
Thermal neutrons ($E \leq 0.1$ eV)	1.6 ± 0.1	0.50 ± 0.05	98
Epithermal neutrons (0.1 eV $< E <$ 1 MeV)	1.6 ± 0.1	0.8 ± 0.2	3.2
Fast neutrons ($E \geq 1$ MeV)	4 ± 1	0.55 ± 0.15	1.1
Total of simulation		2.05 ± 0.25	2.7
Experiment		2.19 ± 0.17	3.2

Table 7
Comparison between data and simulation for the study of neutron contamination in the NEMO 3 detector.

ID	% of events with at least one PMT (simu output)	Associated trigger efficiency (%)	% of events with at least two PMTs (simu output)	Associated trigger efficiency (%) [see caption]
1	96.1	96.1 ± 1.0	56.8	56.8 ± 0.7 [100]
2	73.6	73.0 ± 0.9	22.7	22.7 ± 0.5 [100]
3	65.7	63.5 ± 0.8	16.9	16.3 ± 0.4 [96.7]
4	58.7	56.0 ± 0.8	13.8	12.9 ± 0.4 [94.0]
5	79.4	60.0 ± 0.8	20.7	15.4 ± 0.4 [74.5]

Table 8

Results of simulations giving trigger efficiencies relative to the number of events coming from: ID=1- $\beta\beta 0\nu$ from molybdenum foils; ID=2- $\beta\beta 2\nu$ from molybdenum foils; ID=3- Thallium impurities from molybdenum foils; ID=4- Bismuth impurities from molybdenum foils; ID=5- Bismuth impurities from gas. The number of generated events for each ID is 10000. The proportion of accepted simulated events are given in the first (respectively third) column for at least one (respectively two) PMT(s). The lost is mainly due to geometrical cuts. The proportion of accepted events after applying trigger criteria are given in second and fourth column: it represents the trigger efficiency (the error bars are statistical uncertainties). The efficiency relative to the number of events with exactly two fired PMTs is the number between squared brackets in the last column.

Trigger conditions	Event type	Counting rate (Hz)
≥ 1 triggered PMT with $E_{PMT} > 150$ keV	PMT singles	580
≥ 1 track	GG singles	65
$\geq$ (1 triggered PMT + 1 track) with $E_{PMT} > 150$ keV	(e), (e, e), (e, $N\gamma$), (e, e, $N\gamma$), with $N \geq 1$	7.4
$\geq$ (2 triggered PMTs + 1 track) with $E_{PMTs} > 150$ keV	(e, e), (e, $N\gamma$), (e, e, $N\gamma$), with $N \geq 1$	1.15

Table 9

Different types of counting rate using parts of $\beta\beta$ trigger

Type of event	Proportion (in %)
$1e^-$, 0γ-ray	7.7
$1e^-$, $N\gamma$-rays, $N \geq 1$	2.0
$1e^+$, 0γ-ray	1.4
$1e^+$, $N\gamma$-rays, $N \geq 1$	0.66
e^+e^- pairs	1.5
one crossing e^-	1.1
$2e^-$, 0γ**-ray**	**0.15**

Table 10
Proportion of different types of events in a $\beta\beta$ run. Except for one crossing electron events, electrons and positrons are coming from the source foils and associated trajectories are reconstructed with only one track. Thus missing events are for example backscattering events, or electrons going back to the source foils, with at least two reconstructeds tracks in associated trajectories.

Bloc type	Associated PMT	Corrected resolution $\frac{\sigma_E}{E}$ at 1 MeV (in %)
IN	3"	7.3 ± 0.1
EC	5"	6.0 ± 0.1
EE	5"	6.0 ± 0.1
L1	3"	7.1 ± 0.2
L2	3"	7.1 ± 0.2
L3	3"	7.5 ± 0.2
L4	5"	6.3 ± 0.2

Table 11
Energy resolutions corrected from impact position on scintillators ($\frac{\sigma_E}{E}$ values at 1 MeV, in %).

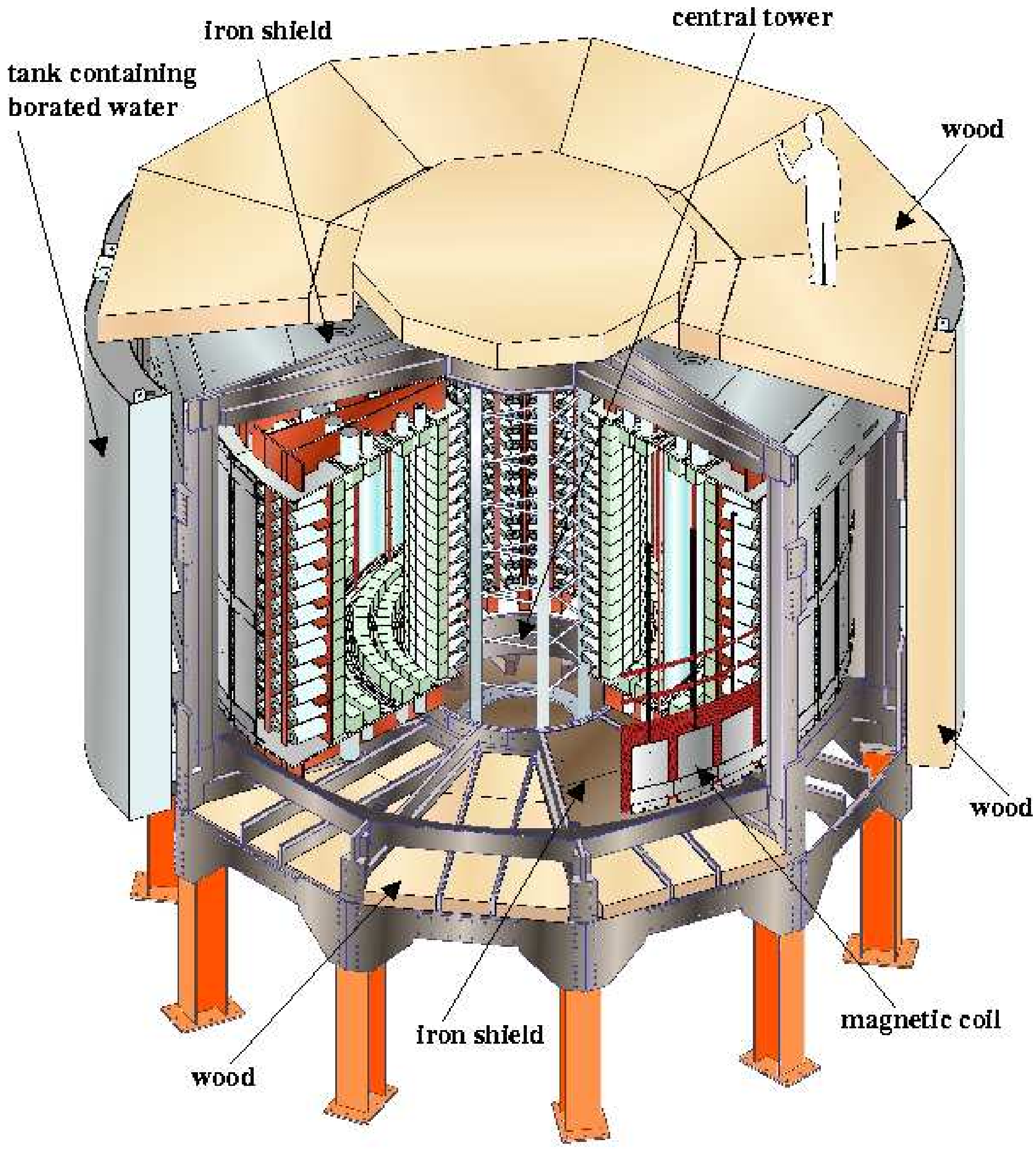

Fig. 1. Layout of the NEMO 3 detector, surrounded with coil, iron γ-ray shield, and the three different types of neutron shield, composed of water tanks, wood and paraffin (the last one is not shown on the picture).

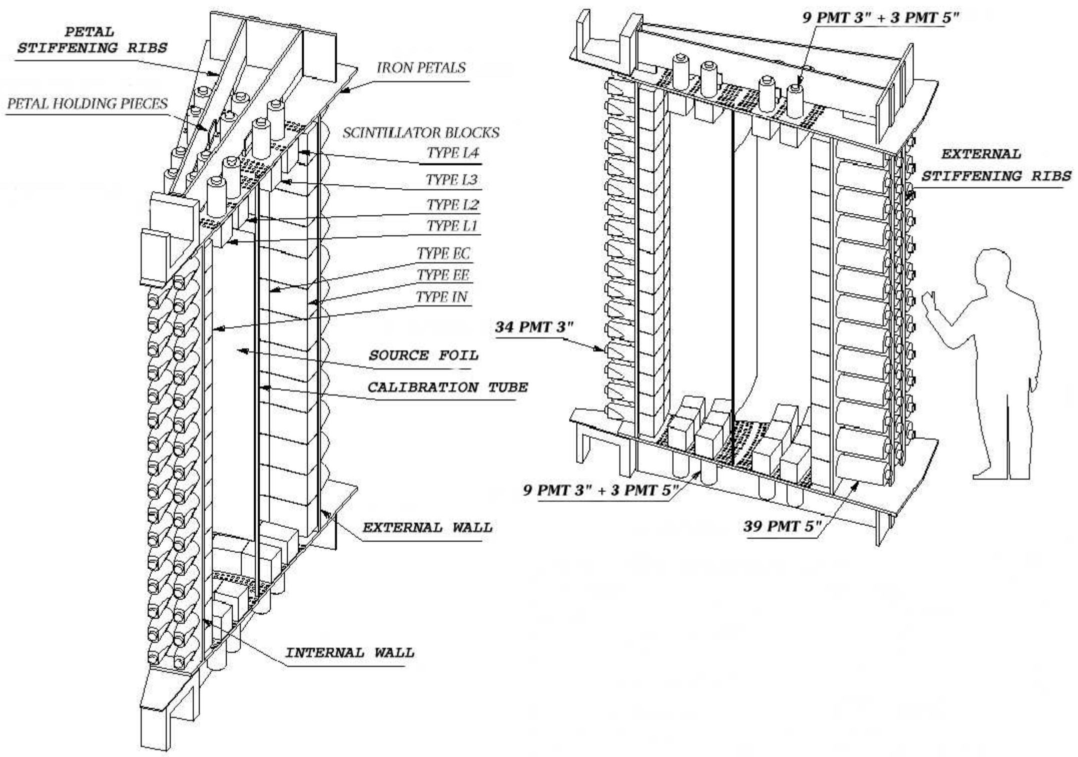

Fig. 2. One sector of NEMO 3 with details on the source foil, scintillator blocks and photomultipliers. The Geiger cells are located between the internal and external walls. L4, L3,... IN means different shapes of scintillator blocks.

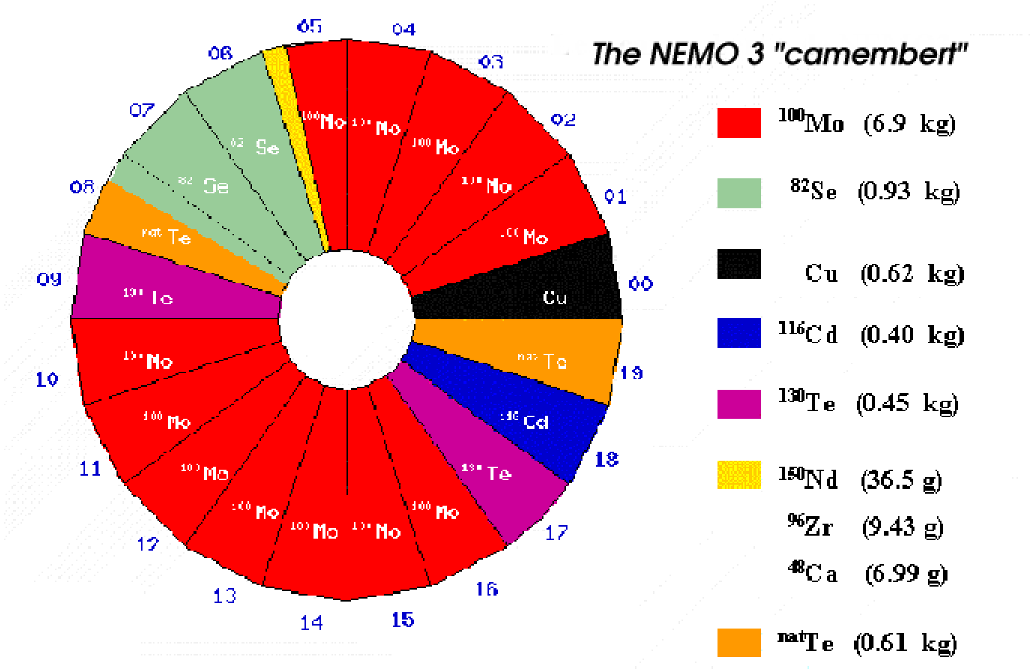

Fig. 3. The source distribution in the 20 sectors of NEMO 3.

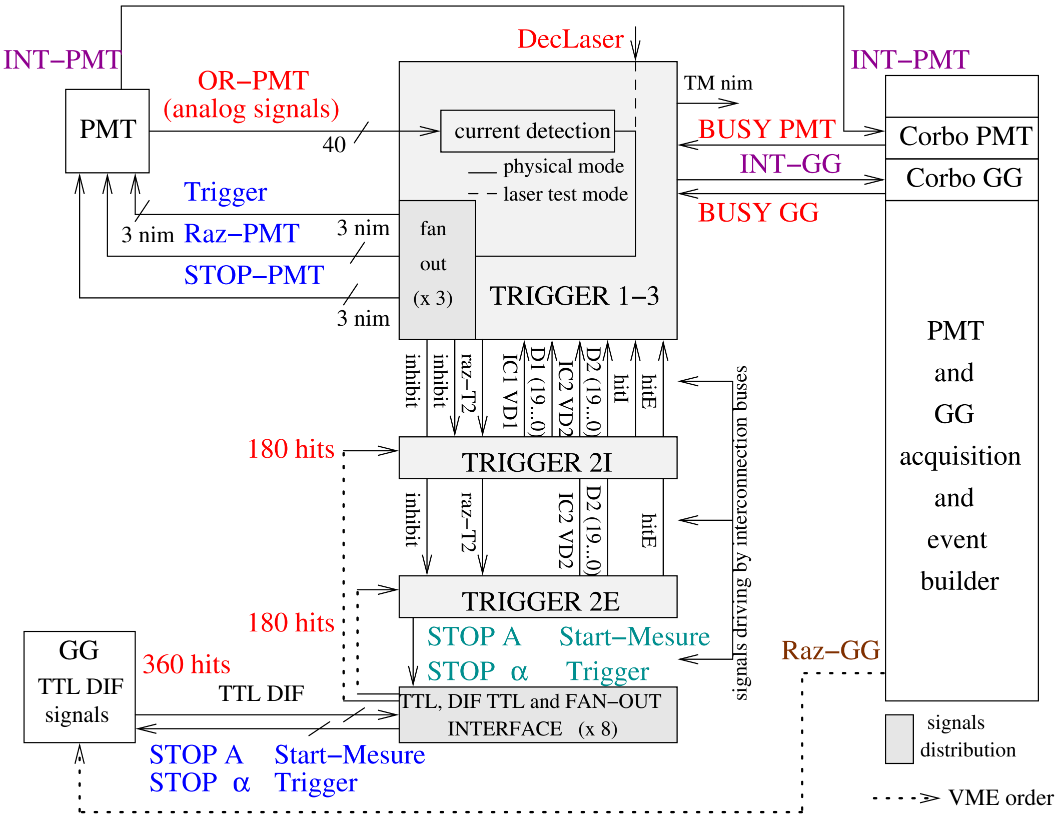

Fig. 4. Synopsis of the NEMO 3 trigger system.

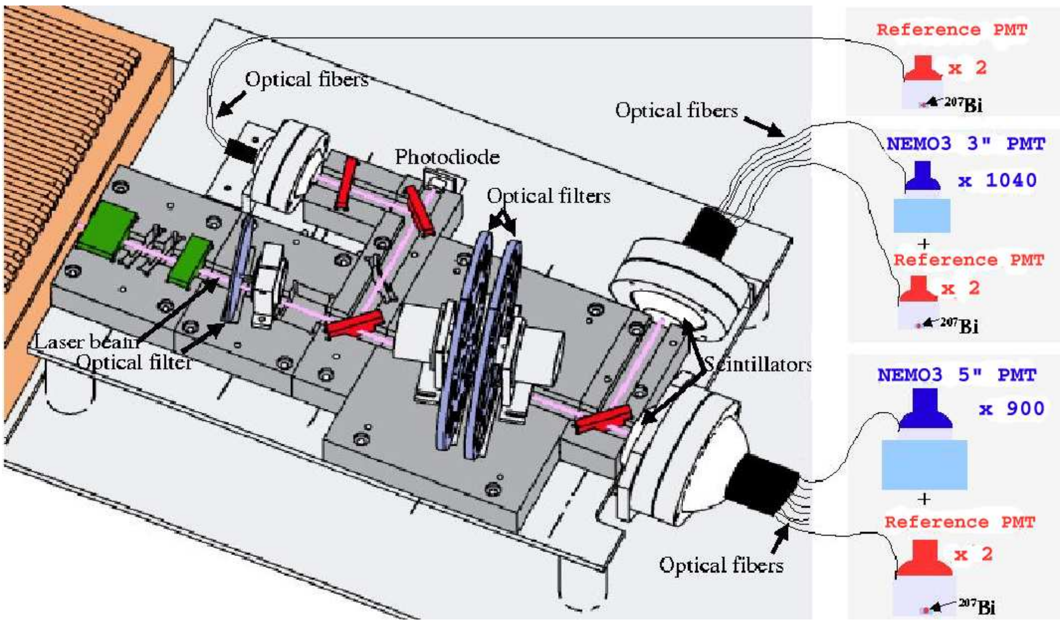

Fig. 5. The laser calibration system.

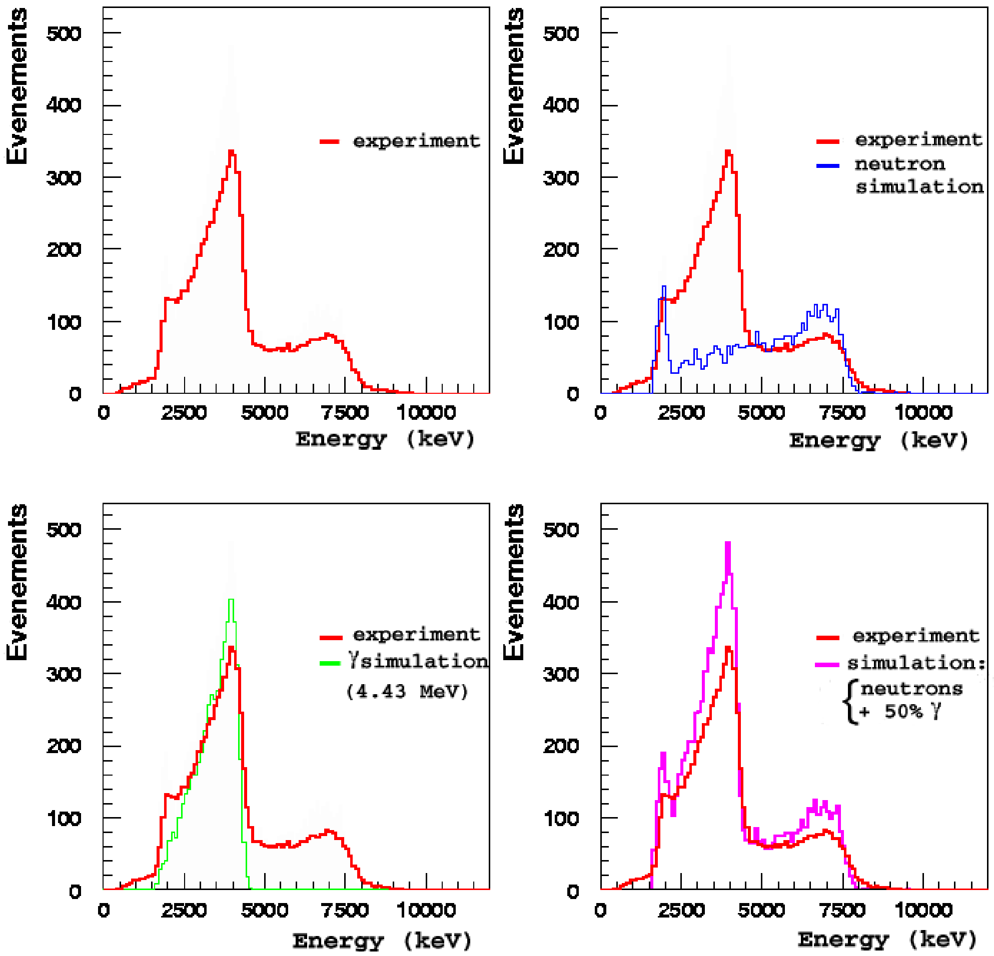

Fig. 6. Comparison between simulation and data with magnetic field and no shield, for one crossing electron events (with or without γ-rays), obtained with a neutron Am-Be source. See text for more details.

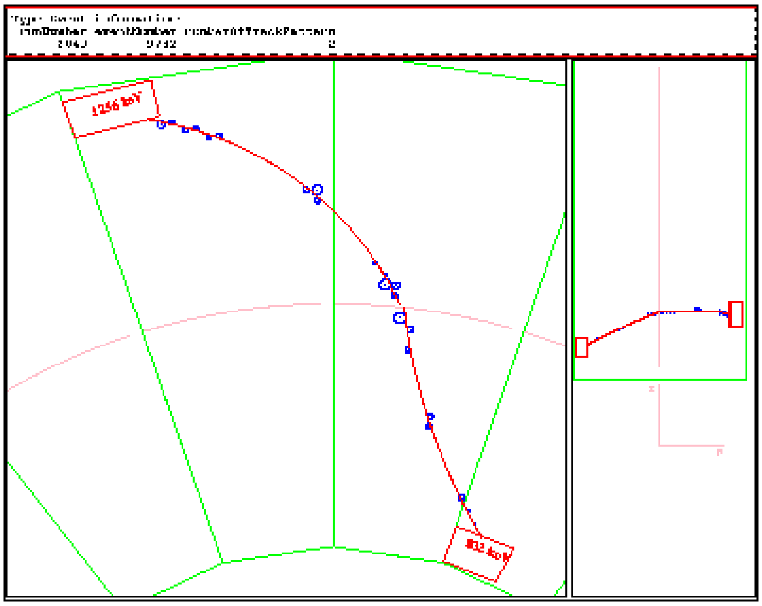

Fig. 7. Two e^- event produced in molybdenum source foil (sector 4). Left part of this figure shows a zoom of the transverse top view of NEMO 3, while the right part presents the associated longitudinal view. Circle radius correspond to the transverse distance from anode wire for each fired cell. Electrons, in time, have respective energy of 1256 keV (in sector 5) and 832 keV (in sector 3).

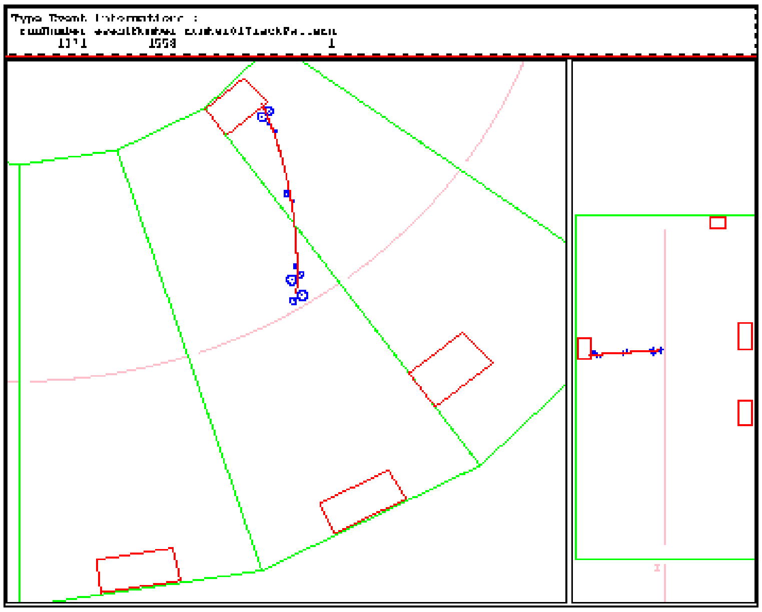

Fig. 8. A $e^-\gamma\gamma\gamma$ background event produced in molybdenum foil (sector 16).

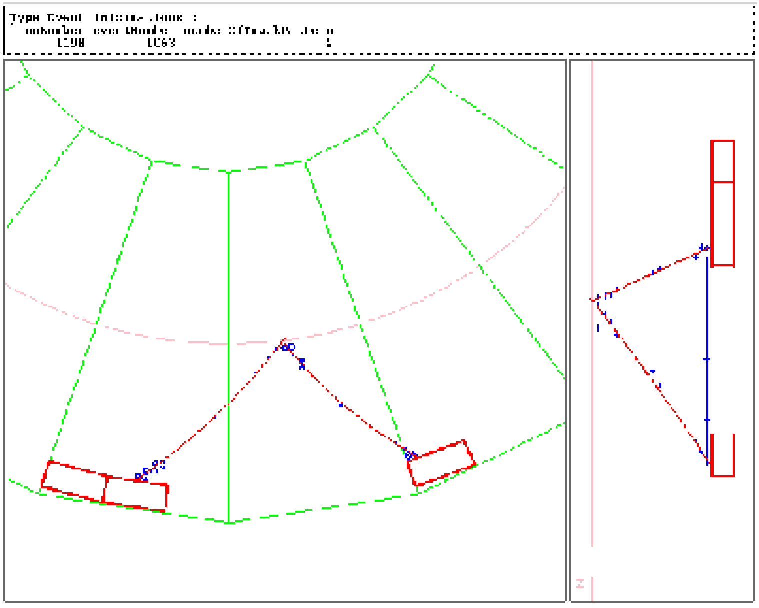

Fig. 9. A e^+e^- background event produced in a molybdenum foil (sector 15). Note the tracks of opposite curvature and the presence of gamma-rays. Large error bars in longitudinal view correspond to cells with missing cathodes.

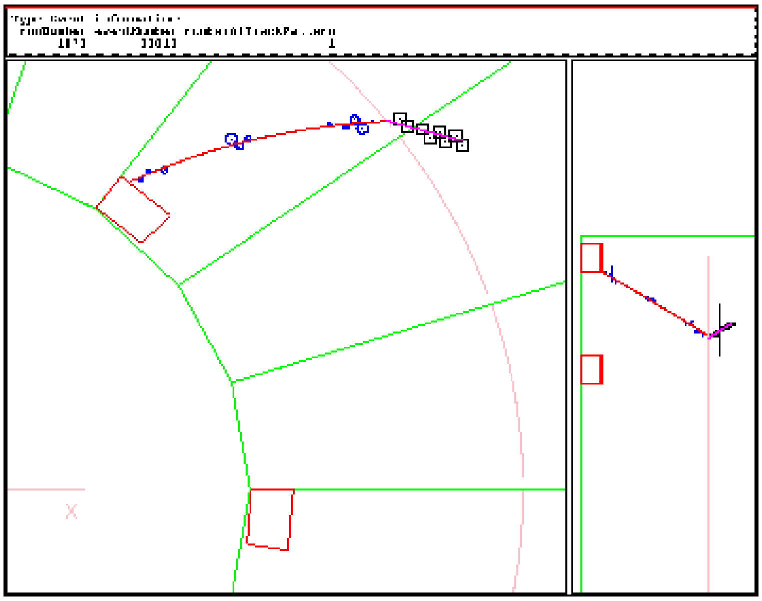

Fig. 10. Decay of some internal contamination producing a single electron event coming from molybdenum source foil (sector 2) followed by a delayed alpha particle, which is the short straight track represented by open squares.

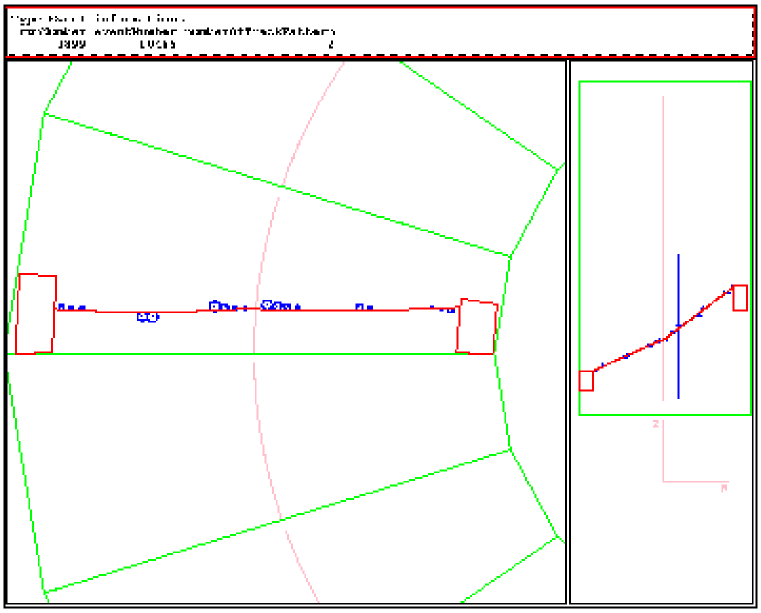

Fig. 11. Example of an external source of background: it is a view of high energy crossing electron background event, which is most likely produced by a high-energy γ-ray emitted after a neutron capture in the copper frame. This type of events is used to establish reconstruction formulae for transversal and longitudinal positions in the tracking detector. It can be distinguished from back-to-back electrons events emitted from the source foils by time-of-flight measurements (see paragraph 3.4).

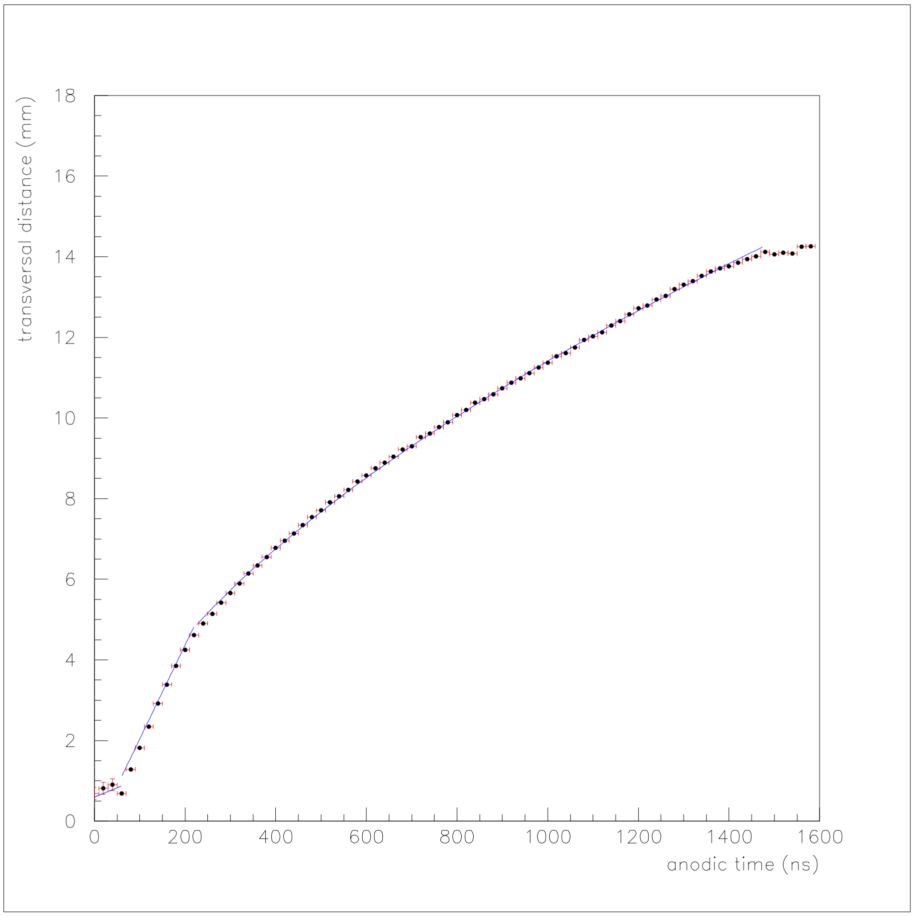

Fig. 12. Transverse distance to the fitted track $r_\perp$ (in mm) as a function of anodic time t_A (in ns) obtained with high energy crossing events ($e_{cross} > 4.5$ MeV).

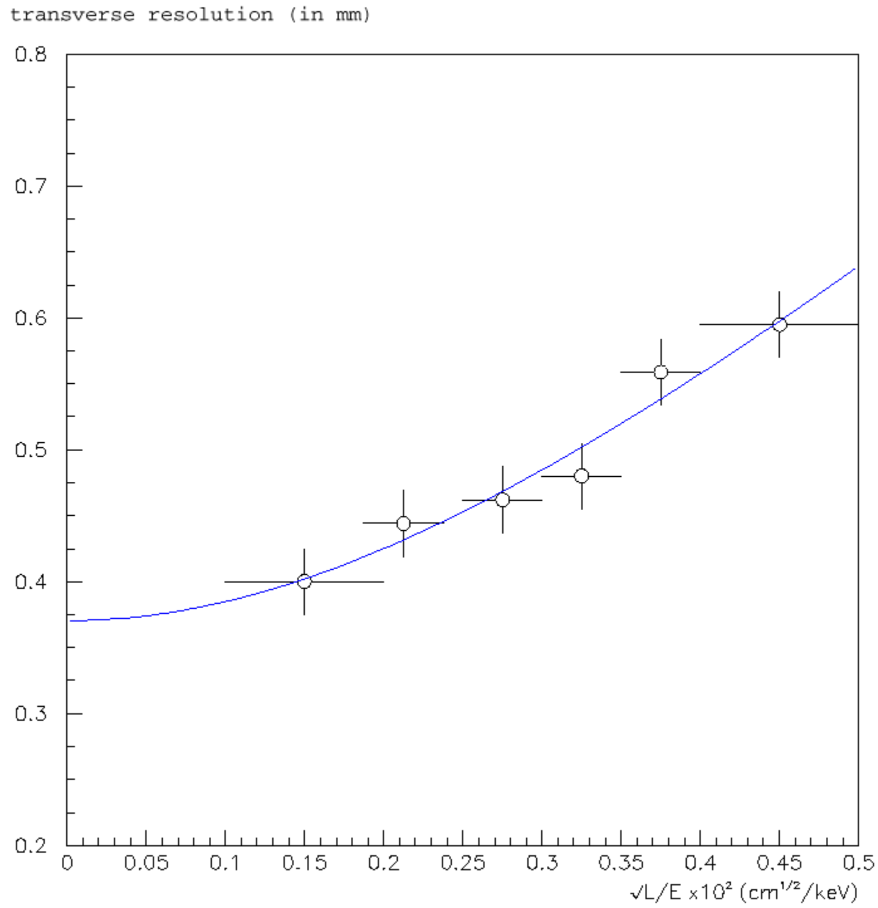

Fig. 13. Distribution of transverse resolution per cell $\sigma_\perp$ (in cm) as a function of the variable $\sqrt{L_{track}}/E$. Associated curve is the result of the fit given by $\sigma_\perp = \sqrt{\sigma_{int}^2 + k\,(\sqrt{L_{track}}/E)^2}$.

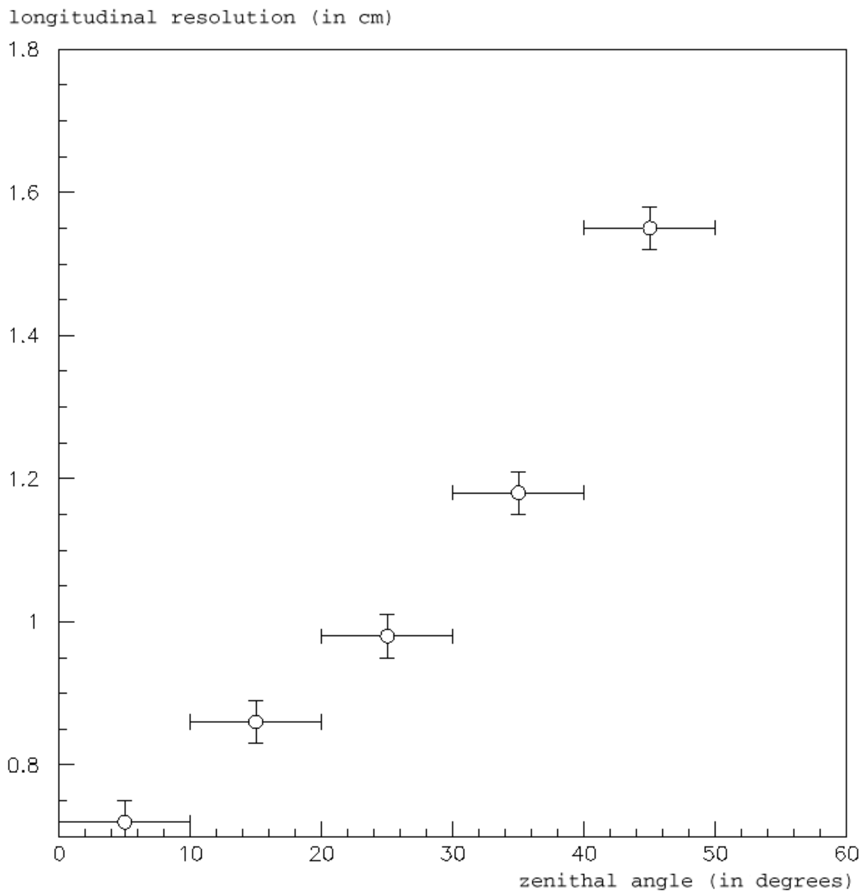

Fig. 14. Distribution of longitudinal resolution per cell $\sigma_{//}$ (in cm) as a function of zenith angle θ (in degrees).

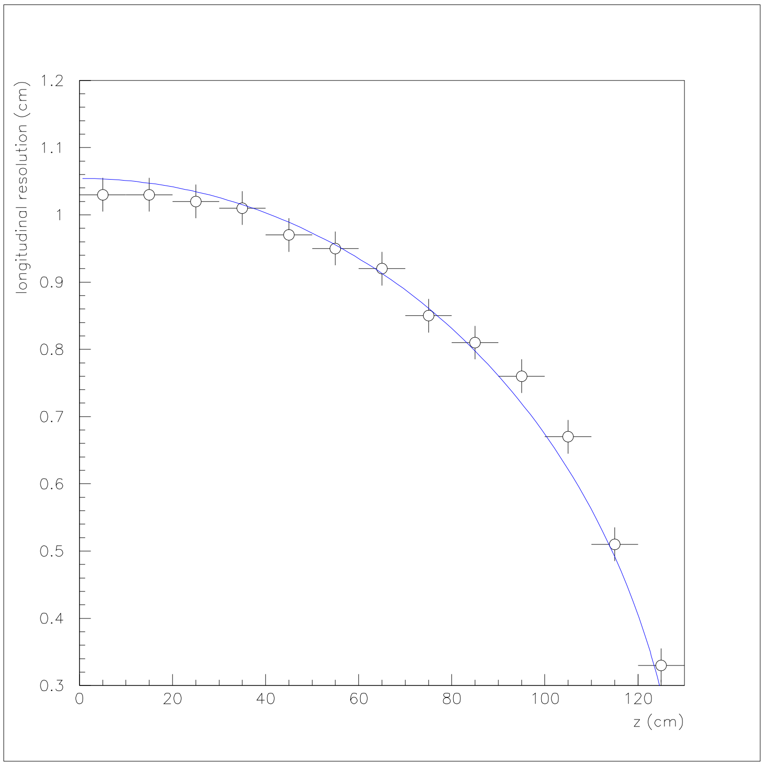

Fig. 15. Distribution of longitudinal resolution per cell $\sigma_{//}$ (in cm) as a function of longitudinal position z (in cm). Associated curve is the result of the fit given by $\sigma_{//} = \sigma_0 \sqrt{1 - (2z/L_{eff})^2}$.

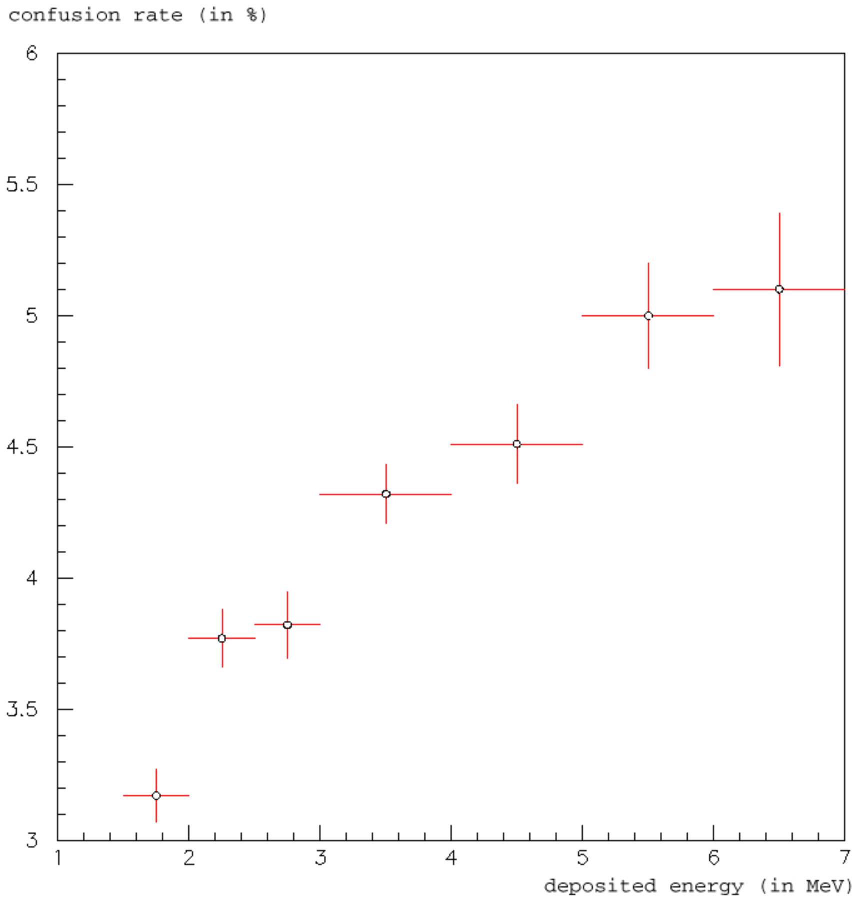

Fig. 16. Distribution of electron reconstruction error rate as a function of electron energy. The e^+e^- confusion rate is around 3% at 1 MeV.

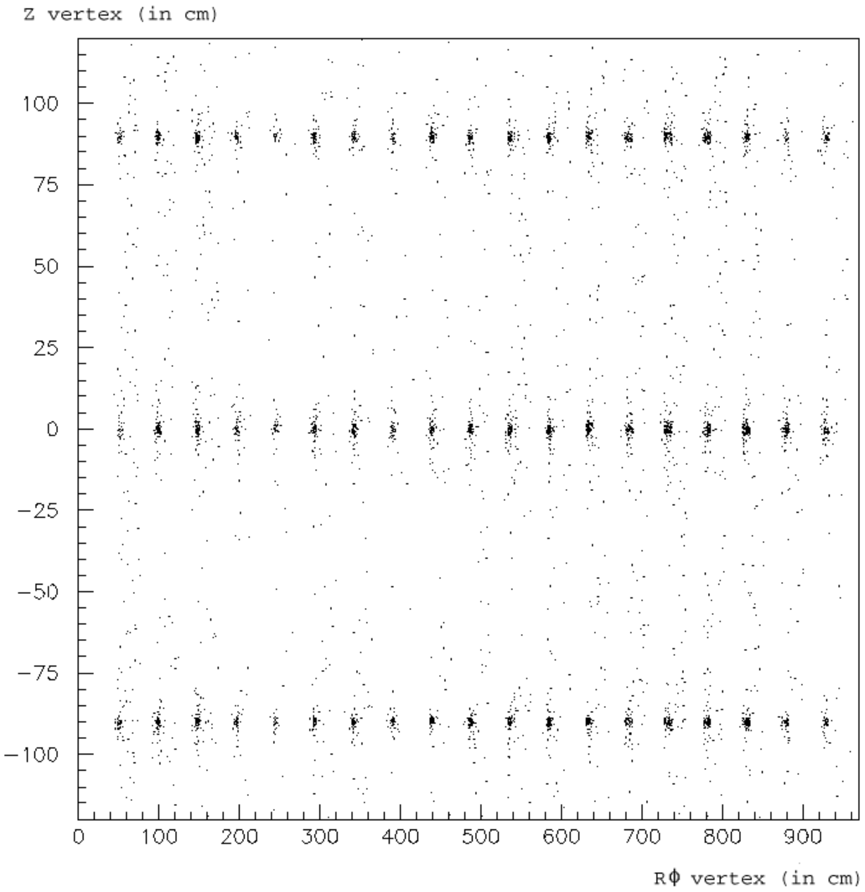

Fig. 17. Distribution of reconstructed vertices for the 60 positions of calibration ^{207}Bi sources, in the $1e^-$ channel.

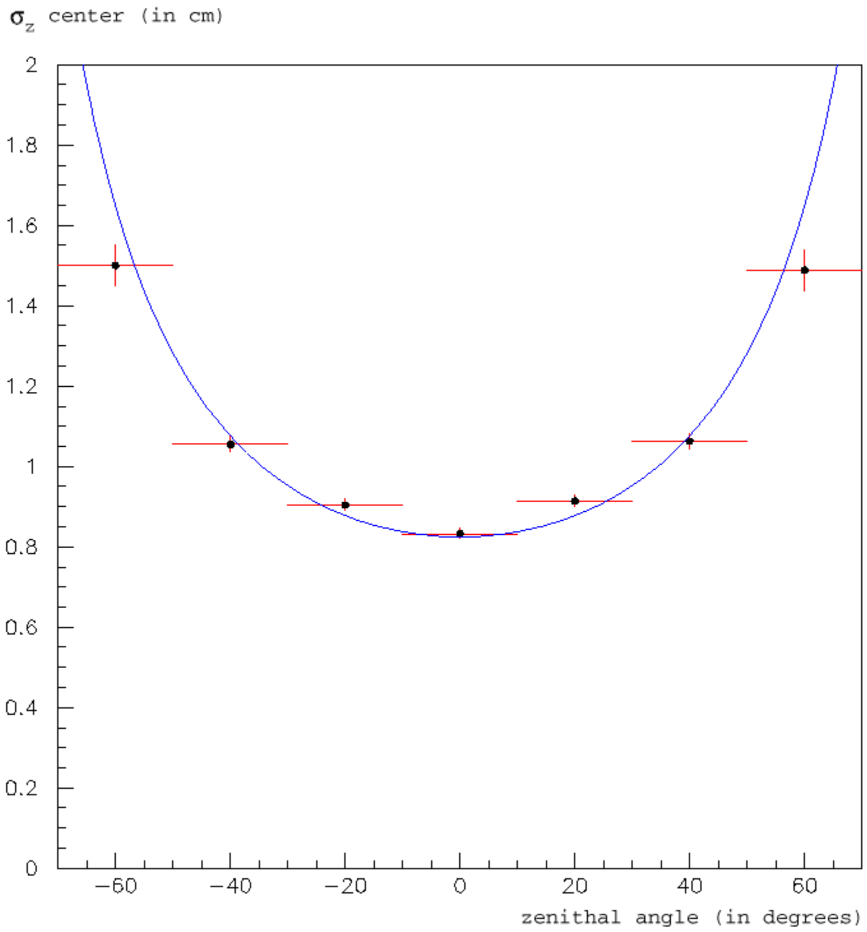

Fig. 18. Distribution of vertex longitudinal resolution σ_Z (in cm) as a function of zenithal angle θ (in degrees), with a $\sigma_0'/cos\theta$ adjustment (obtained for ^{207}Bi sources in central position).

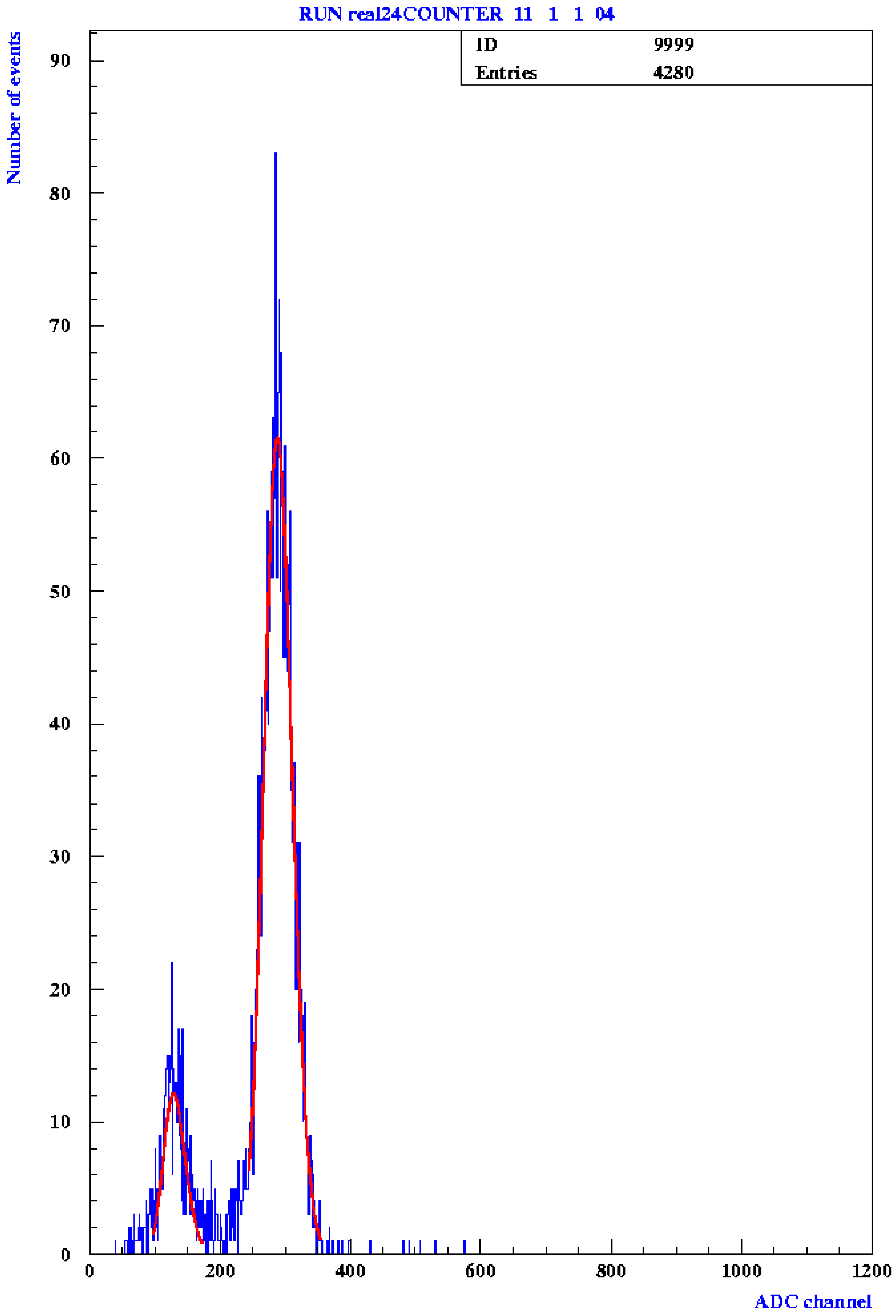

Fig. 19. Fit of the 976 keV and 482 keV peak positions coming from ^{207}Bi decays for one counter ($\sim$ 3 keV/channel).

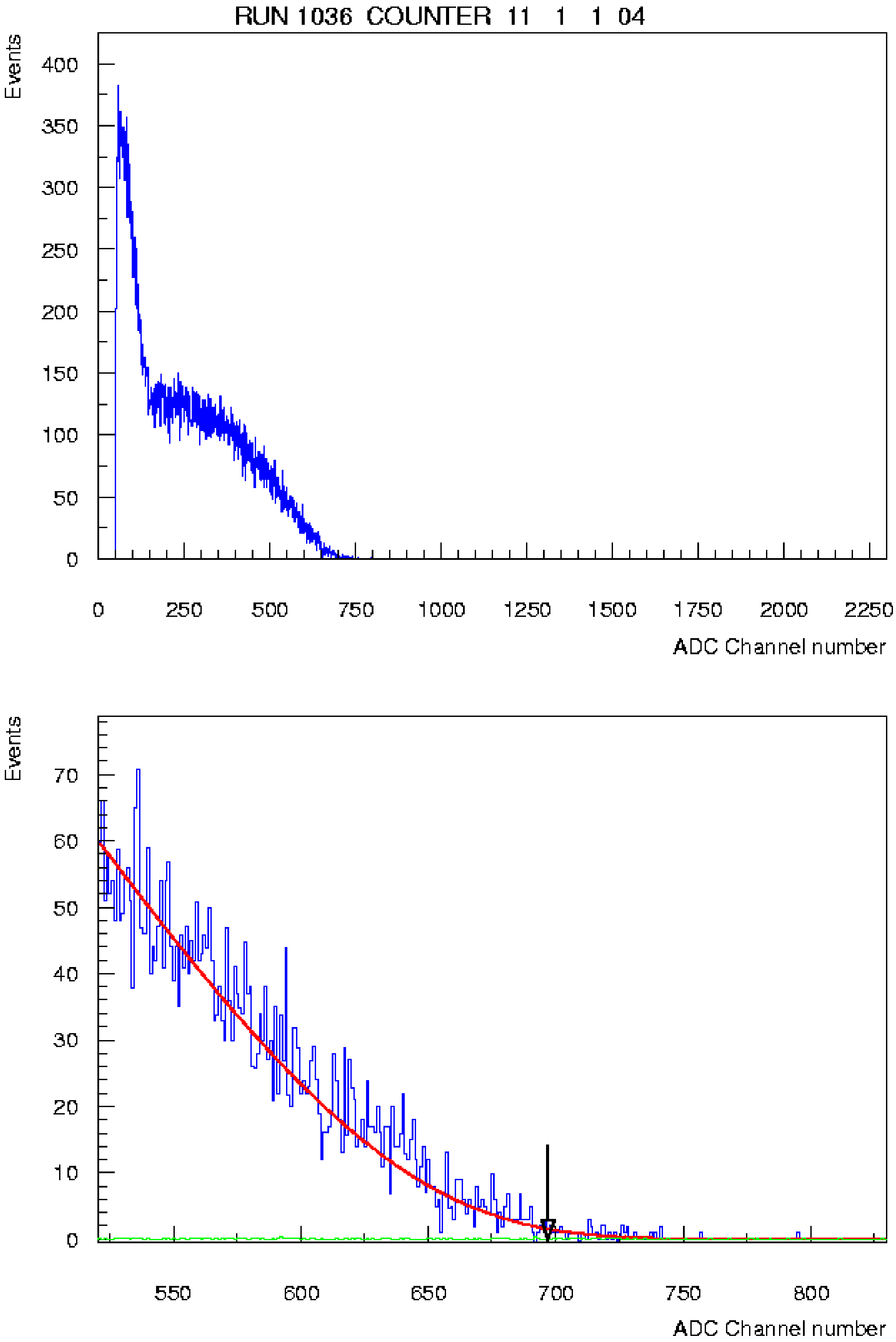

Fig. 20. Typical example of beta end-point adjustement (2.283 MeV) in energy spectrum associated to ^{90}Sr calibration source decays for the same counter ($\sim$ 3 keV/channel). The fit to the high-energy tail of the spectrum is made with a function describing the shape of a single β spectrum of ^{90}Sr, convoluted by the energy resolution function $\sigma(E)$ and taking into account the mean energy loss of the electrons.

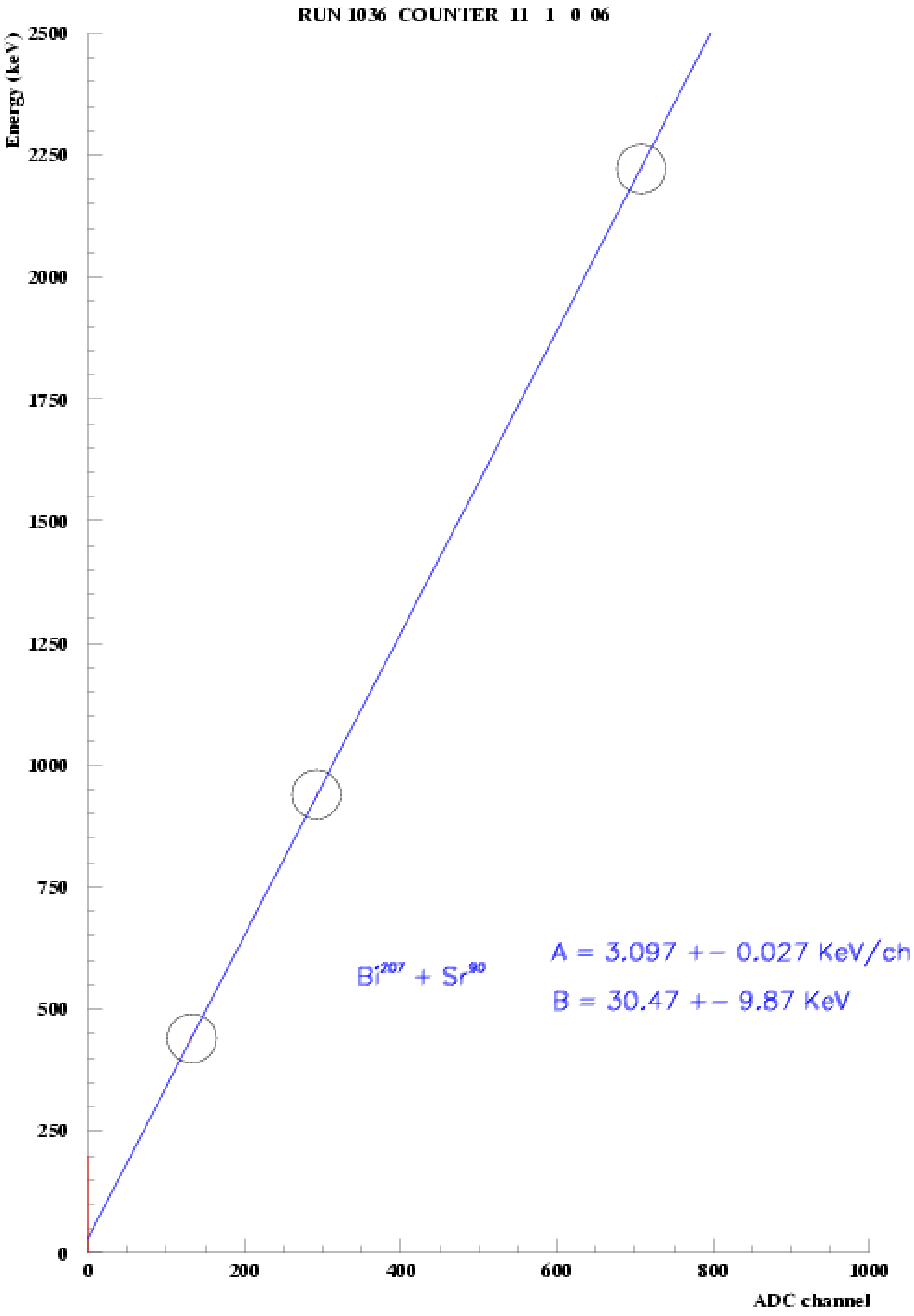

Fig. 21. Typical example of mean counter behavior showing calibration fit using 3 points coming from ^{207}Bi and ^{90}Sr data, which is used to obtain calibration parameters (a and b) and energy-channel relation for each counter ($\sim$ 3 keV/channel).

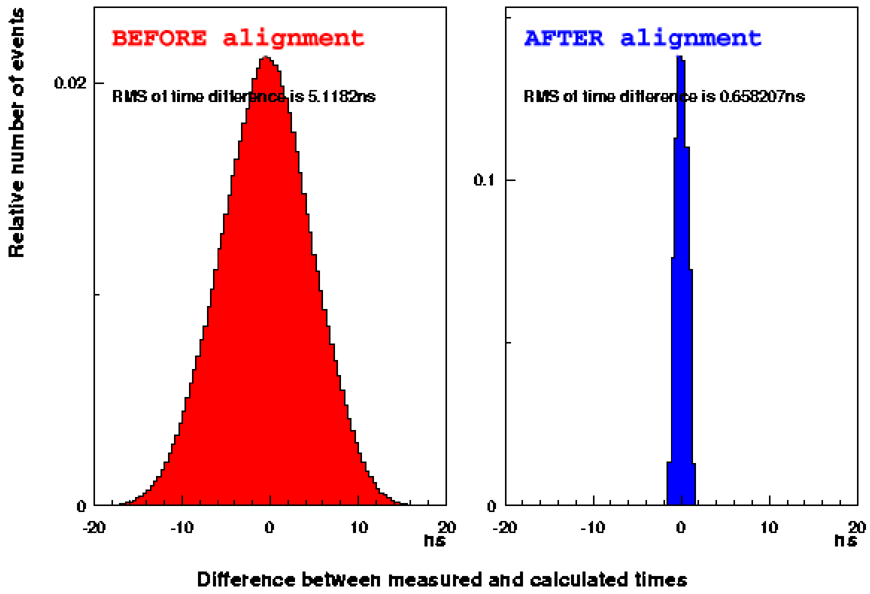

Fig. 22. Distribution of the arrival time difference in the counters before and after alignment with ^{60}Co calibration sources. The distribution after alignment has a resulting RMS of $\sim$ 700 ps.

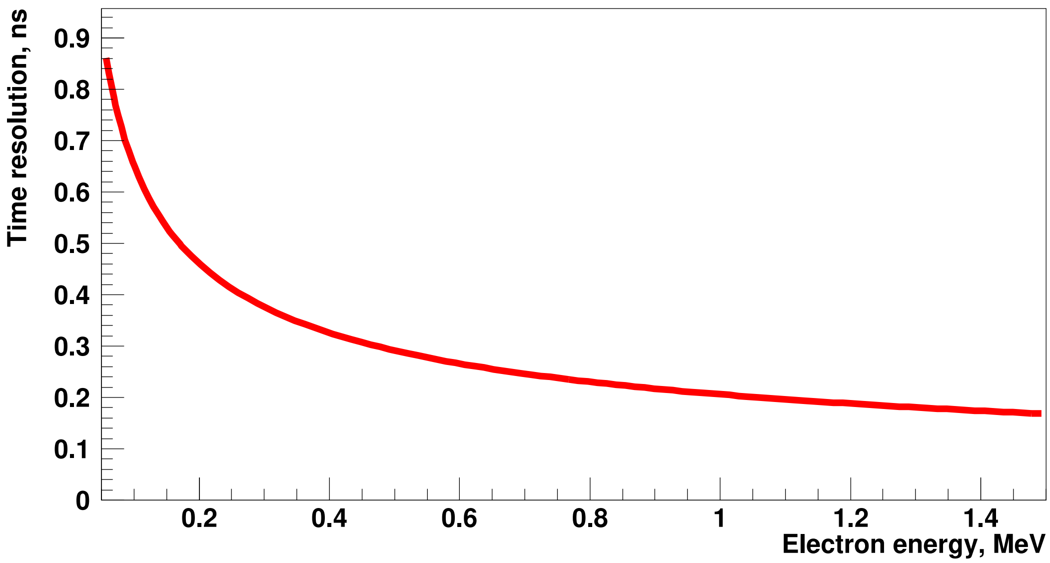

Fig. 23. Time resolution (in ns) as function of the electron energy (in MeV).

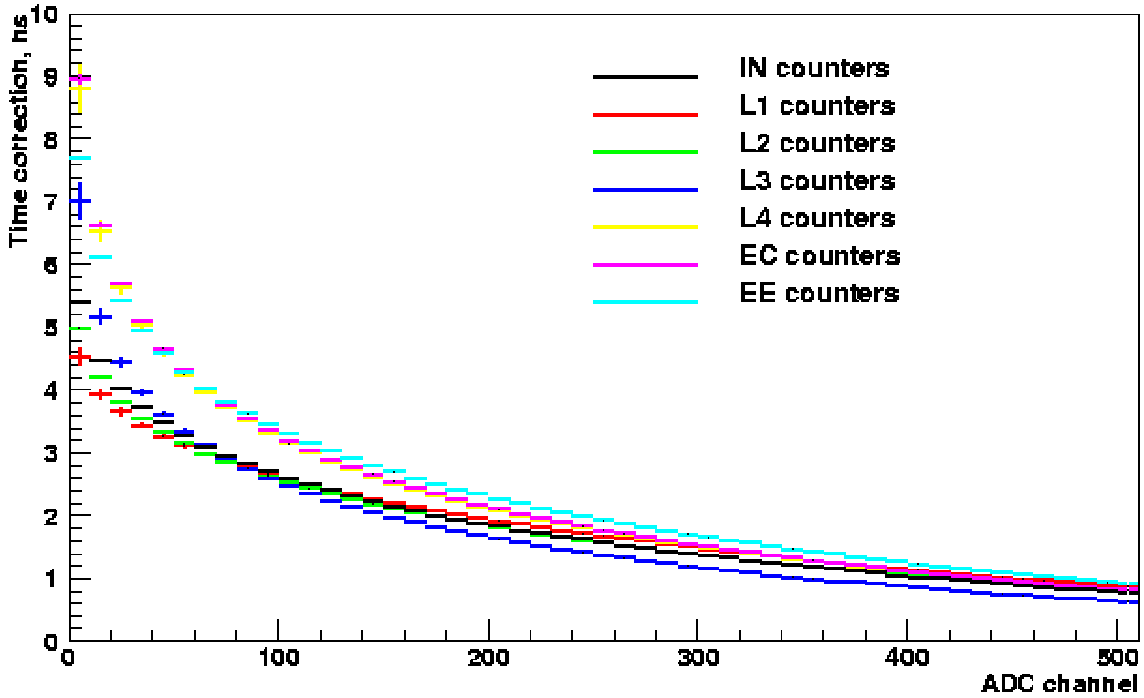

Fig. 24. Time correction (in ns) as a function of adc (in channel) for the different types of counters ($\sim$ 3 keV/channel).

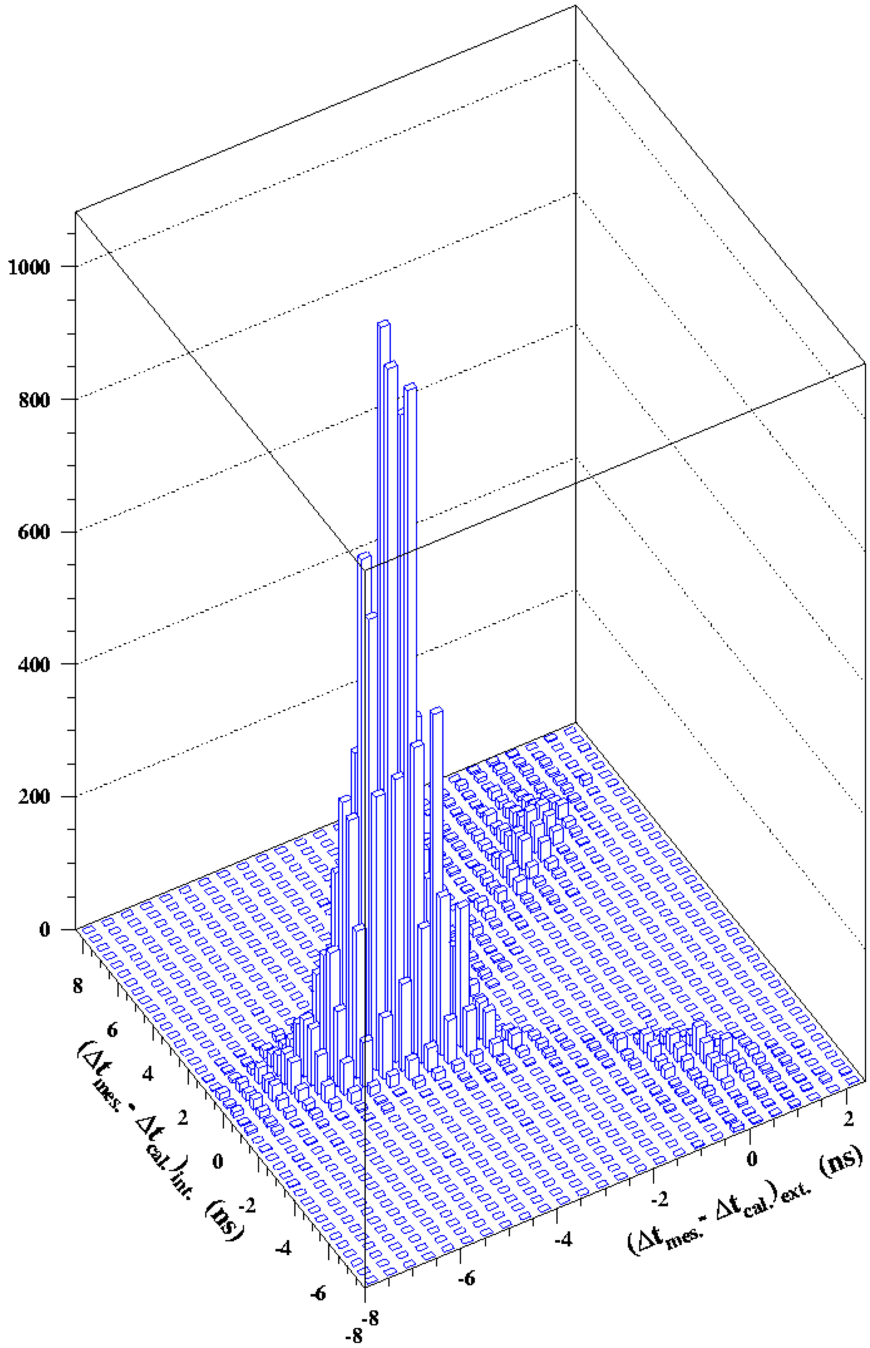

Fig. 25. $(\Delta T_{meas} - \Delta T_{cal})_{int}$ vs $(\Delta T_{meas} - \Delta T_{cal})_{ext}$ for 2 track events from ^{100}Mo source foils. See text for more details.

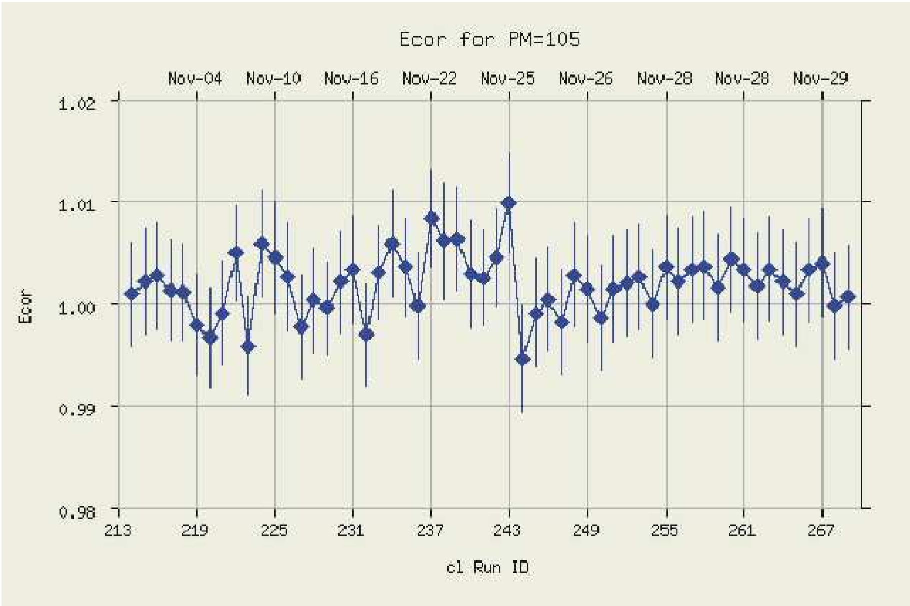

Fig. 26. Typical example of long term (one month) stability for energy correction parameter e_{corr} of one counter.

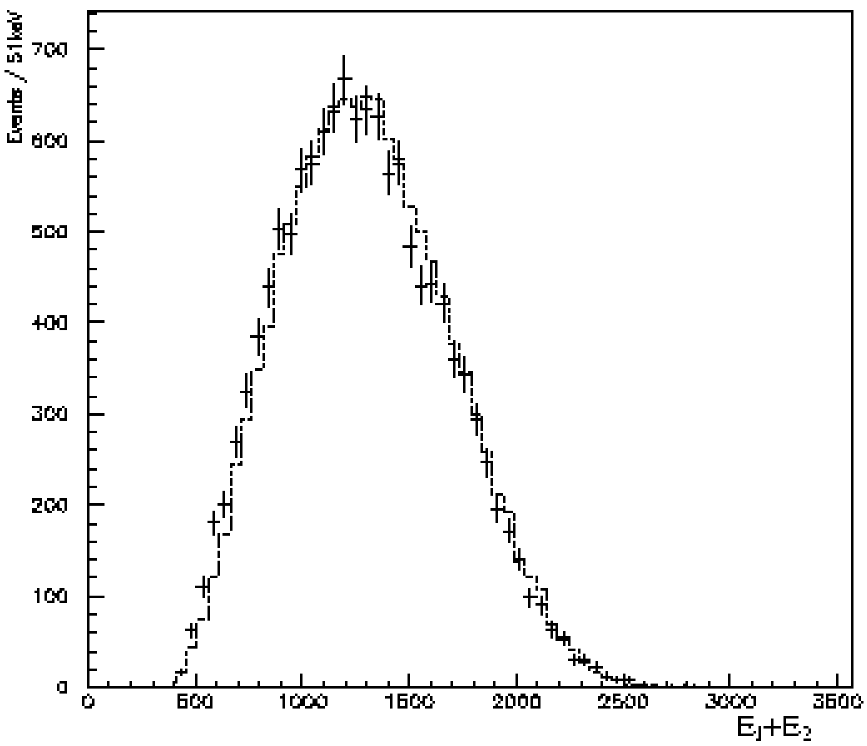

Fig. 27. Distribution of the experimental total energy sum measured with molybdenum sources (background substracted) compared to $\beta\beta 2\nu$ Monte-Carlo. It corresponds to 650 h of data taking in stable conditions, between mid-february and end of march 2003. The number of events is ~ 14000, with a signal to background ratio of 40.

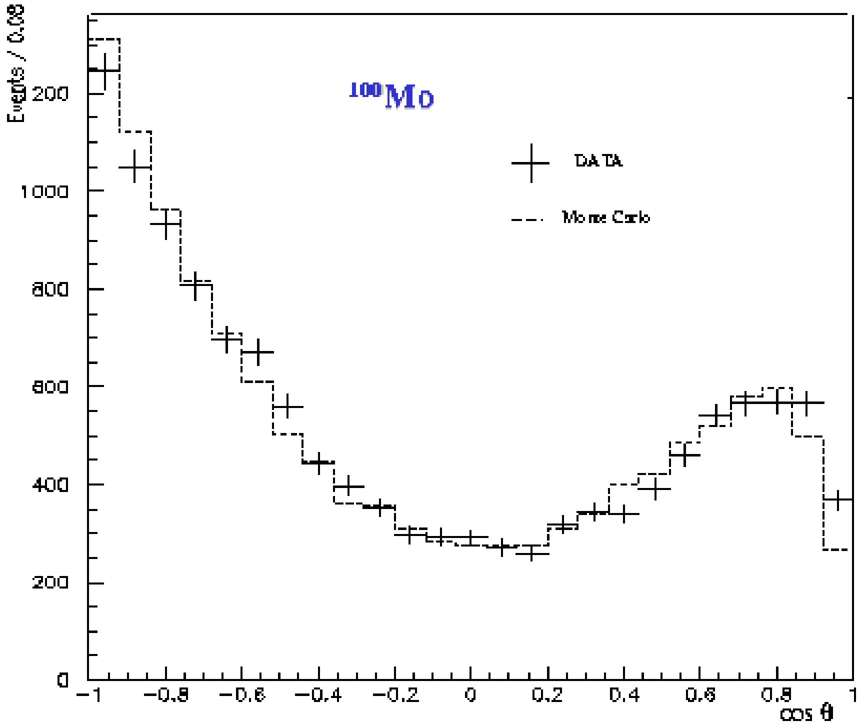

Fig. 28. Experimental angular distribution for molybdenum sources compared to $\beta\beta 2\nu$ Monte-Carlo. It corresponds to the same data than Fig. 27.